metals

MDPI

Article

Experiments and Simulations on the Low-Temperature Reduction of Iron Ore Oxide Pellets with Hydrogen

Róbert Findorák [1,*], Zuzana Miškovičová [1], Jaroslav Legemza [1], Róbert Dzurňák [1], Branislav Buľko [1], Peter Demeter [1], Andrea Egryová [2] and Róbert Maliňák [2]

[1] Institute of Metallurgical Technologies and Digital Transformation, Faculty of Materials, Metallurgy and Recycling, Technical University of Kosice, Letna 1/9, 042 00 Kosice, Slovakia; zuzana.miskovicova@tuke.sk (Z.M.); jaroslav.legemza@tuke.sk (J.L.); robert.dzurnak@tuke.sk (R.D.); branislav.bulko@tuke.sk (B.B.); peter.demeter@tuke.sk (P.D.)

[2] U. S. Steel Košice, s.r.o., 044 54 Kosice, Slovakia; aegryova@sk.uss.com (A.E.); rmalinak@sk.uss.com (R.M.)

* Correspondence: robert.findorak@tuke.sk

Abstract: This article examines the low-temperature reducibility of four types of iron ore pellets in a pure hydrogen atmosphere, with the aim of understanding the thermodynamic aspects of the process. The research focuses on optimizing conditions for pellet reduction in order to reduce CO_2 emissions and improve iron production efficiency. Experimental tests were conducted at temperatures of 600 °C and 800 °C, supplemented by thermodynamic simulations predicting the equilibrium composition and energy requirements. Chemical and microstructural analyses revealed that porosity, mineralogical composition, and phase distribution homogeneity significantly affect reduction efficiency. High-quality pellets with low SiO_2 content demonstrated the best reduction ability, while fluxed pellets with the presence of calcium silicate ferrites and pellets with a higher content of SiO_2 showed lower reduction potential due to the presence of hard-to-reduce phases such as calcium silicate ferrites and iron silicates. The results highlight the importance of controlling process conditions and optimizing pellet properties to enhance the reduction process and minimize environmental impacts. This study provides valuable insights for the application of hydrogen reduction in industrial conditions, contributing to the decarbonization of the metallurgical industry.

Keywords: iron ore pellets; reduction with hydrogen; decarbonization

check for updates

Received: 3 February 2025
Revised: 27 February 2025
Accepted: 2 March 2025
Published: 6 March 2025

Citation: Findorák, R.; Miškovičová, Z.; Legemza, J.; Dzurňák, R.; Buľko, B.; Demeter, P.; Egryová, A.; Maliňák, R. Experiments and Simulations on the Low-Temperature Reduction of Iron Ore Oxide Pellets with Hydrogen. *Metals* **2025**, *15*, 289. https://doi.org/10.3390/met15030289

Copyright: © 2025 by the authors. Licensee MDPI, Basel, Switzerland. This article is an open access article distributed under the terms and conditions of the Creative Commons Attribution (CC BY) license (https://creativecommons.org/licenses/by/4.0/).

1. Introduction

The reduction of iron ore pellets is one of the key steps in iron and steel production, traditionally relying on fossil fuels, primarily coal, as the main source of energy and reducing agent. This process is a significant source of carbon dioxide (CO_2) emissions, with the steel industry contributing approximately 7–9% of global anthropogenic greenhouse gas emissions. In the context of global efforts to decarbonize industry and meet the climate targets of the Paris Agreement, alternative technological solutions are being sought to achieve significant emission reductions without compromising productivity and product quality. One of the most promising approaches to decarbonizing the metallurgical industry is replacing carbon with hydrogen as the reducing agent in the iron ore pellet reduction process [1–5].

Hydrogen is considered an environmentally friendly solution because its reduction product is water (H_2O), thereby eliminating the production of CO_2. The use of hydrogen also presents a synergistic opportunity for integration with renewable energy sources,

which can provide its production through electrolytic processes. The fundamental chemical reactions for the reduction of iron oxide—Fe_2O_3 and Fe_3O_4—with hydrogen are already well known; however, the implementation of this technology at an industrial scale requires a detailed understanding of the kinetic, thermodynamic, and mechanistic aspects of the process. Important factors include reaction temperature, hydrogen concentration, the properties of the input pellets (e.g., microstructure and porosity), as well as potential interferences caused by the presence of impurities [1–5].

Based on a literature review and analysis of experimental and modeling studies, key factors influencing the hydrogen reduction of iron ore pellets were identified. Temperature has a crucial impact on the process kinetics and the pellet microstructure. At temperatures of 700–800 °C, micropores dominate, while at 900–1000 °C, macropores and cracks form, which facilitate the diffusion of reducing gases and increase the reduction rate [6–9]. Complete reduction of Fe_2O_3 to metallic iron is achieved at temperatures above 900 °C, with higher temperatures accelerating the transition between the phases $Fe_2O_3 \rightarrow Fe_3O_4 \rightarrow FeO \rightarrow Fe$ [10,11]. Yan Ma et al. observed significant heterogeneity in the reduction rate between the surface and internal parts of the pellets during hydrogen reduction at 700 °C. The surface layer reached 88% α-iron, while the center exhibited a reduction level of only 4%. Thus, the reduction of pellets is a heterogeneous process, and not all parts of the pellet are reduced uniformly [12]. The outer layers are reduced more rapidly, while the core of the pellets remains partially unreduced, especially at lower temperatures [9]. Changes in microstructure, such as the formation of cracks and pore expansion, influence the subsequent reduction stages and can affect the final quality of the reduced material. This phenomenon is particularly significant at high temperatures, where structural changes become more pronounced and can impact the pellet strength [13]. The pores provide pathways for hydrogen transport, but they can also serve as sites for stress formation and cracking [12]. The porosity is also influenced by the content of gangue components such as SiO_2, Al_2O_3, and MgO. Gangue oxides significantly affect the mechanical properties of the pellets. For example, an increasing content of Al_2O_3 and MgO increased porosity and decreased strength, while a higher SiO_2 content reduced porosity and increased strength [14].

Water vapor significantly affects the reduction kinetics, particularly at lower temperatures (873 K), where it blocks active sites on the surface of the pellets and slows down the process. At higher temperatures (>1073 K), the influence of water vapor decreases, but it still affects the pellet microstructure and reduces the process efficiency [9]. Smaller pellets have the advantage of faster gas diffusion and higher reduction rates, while larger pellets may slow down this process [8,15]. At high temperatures, however, the structural integrity of the pellets may deteriorate due to the formation of cracks and sintering [6,10].

Hydrogen demonstrates higher reduction efficiency compared to CO or H_2–CO mixtures. Complete reduction was achieved at 850 °C in a pure hydrogen atmosphere, while mixtures with higher CO content reduced the efficiency of the process [6,10,16]. In the case of syngas with a high CO content, it was found that the reduction rate was lower due to parallel carbonization reactions—the accumulation of carbon on the surface of the pellets [17]. Reduction in pure hydrogen is completed at lower temperatures compared to the use of carbon monoxide [18]. Reduction is most efficient at temperatures between 800 and 1200 °C, as higher temperatures provide sufficient kinetic energy to accelerate the chemical reactions and facilitate a faster transition between the various reduction stages [19,20].

Increasing the hydrogen pressure to 1–8 bar further accelerates the reduction reactions, as this improves the diffusion of hydrogen into the pellet pores, thereby increasing the availability of the active gas for chemical reactions [19–21]. SEM analyses revealed that at high temperatures, dense iron networks form, while at lower temperatures, fine microp-

ores dominate. This directly impacts gas diffusion and the mechanical properties of the pellets [10,15,22]. Increasing hydrogen pressure can be an effective strategy to accelerate the reduction process and promote the formation of structures suitable for further metallurgical processing [21]. Structural changes affect not only the reduction rate but also the properties of the resulting iron. To enhance the efficiency of the reduction process and the quality of the final product, it is crucial to understand and control the internal structural changes of iron ore pellets, particularly porosity and grain morphology, at different temperatures during reduction [12]. Higher pressure can increase the efficiency of the process, but it may require adjusting the pellet microstructure to ensure sufficient mechanical stability [21].

Another topic addressed by the authors in the studies is the monitoring of the swelling index during reduction (RSI), which quantifies the increase in pellet volume during reduction and is influenced by temperature, the reducing atmosphere, and the pellet composition—particularly the composition of gangue components [23,24]. Swelling in a hydrogen atmosphere often leads to larger cracks, which can reduce the quality of the product. The volumetric expansion of pellets during reduction is attributed to changes in their phase composition, primarily during the reduction of hematite to magnetite. Meshram et al. observed that pellet swelling increases with rising temperature. At 750 °C, the swelling remained below 20%, which is considered normal. However, at temperatures of 850 °C and above, swelling exceeding 20% was observed, reaching more than 70% at 950 °C [25]. Monitoring the RSI is important for minimizing structural defects and optimizing reduction processes, particularly when transitioning to hydrogen reduction [26].

Numerical models have identified key variables such as pellet size, porosity, and temperature that influence the reduction kinetics and enable process optimization [16,22]. The use of hydrogen as a reducing agent has the potential to significantly reduce CO_2 emissions, making this technology key for the decarbonization of the steel industry [22,27]. Currently, the possibility of using NH_3 as a reducing agent is also being discussed worldwide [28].

Overall, the literature review shows that the reduction of iron ore pellets with hydrogen is a complex process that requires precise control of process conditions and an understanding of microstructural changes to optimize efficiency and minimize environmental impacts. Surface studies and microstructural analyses provide valuable insights for the development of future technologies and industrial applications that could contribute to the decarbonization of the steel industry.

This article focuses on the reduction of four types of iron ore pellets in a pure hydrogen atmosphere, with the aim of understanding their reducibility and identifying factors that influence the kinetics and thermodynamics of the process. The research combines experimental testing at different temperatures with thermodynamic simulations that evaluate the equilibrium composition and energy requirements of the individual reaction steps. Additionally, the impact of microstructural properties of the pellets, such as porosity, mineralogical composition, and homogeneity, on the overall reduction efficiency is analyzed.

2. Materials and Methods

Four types of industrially used blast furnace pellets were studied. These included two types of high-quality pellets with low SiO_2 content (pellets A and B), with pellet B being fluxed. Pellets C and D represented standard-quality pellets and had a higher SiO_2 content than pellets A and B. The experimental conditions are listed in Table 1.

Table 1. Description of the reduction experiments in the muffle furnace (MP-62, type MARK ESA).

Atmosphere	Inert atmosphere—100% N_2; Isothermic reduction atmosphere—100% H_2
Gas flow	N_2—3 L/min H_2—11 L/min
Used temperatures	600 °C, 800 °C
Measurements of temperature	PtRh10%-Pt thermocouple
Holding time	30 min.
Sample	3 pieces of pellets from each sample

The chemical composition was identified using several methodologies prescribed by ISO, ASTM, and DIN standards, as well as company standards. The applied methods primarily included X-ray fluorescence (XRF) for elements Fe, Mn, Si, Al, Ca, Mg, P, S, and K, atomic absorption spectroscopy (AAS) for elements Fe, Si, Al, Ca, and Mg, infrared spectroscopy (IR) for elements C and S, and titrimetric and gravimetric methods for FeO. The chemical composition was also determined using the Niton XL3 Gold XRF spectrometer (Thermo Fisher Scientific, Waltham, MA, USA) and elemental analysis with the Thermo Scientific ICE 3500 AAS (Thermo Fisher Scientific, Waltham, MA, USA). Sieve analysis was performed using a KVT-U-2 vibration-pendulum sorter with a set of sieves (Přerov, Czech Republic). The phase composition of the analyzed pellets was carried out using X-ray diffraction with the SEIFERT XRD 3003/PTS diffractometer (General Electric Company, Boston, MA, USA). The obtained diffraction patterns were analyzed using the DIFFRACE.EVA program (Search-Match, KARLSRUHE & VIERSEN, Bruker, Billerica, MA, USA) with the PDF2 database and the TOPASsoftware version 4 (Bruker, Billerica, MA, USA). The melting interval was determined through high-temperature microscope images from a Leitz WETZLAR (New York Microscope Company, New York, NY, USA) microscope. For microscopic observation of the samples, a FE SEM MIRA 3 scanning electron microscope (TESCAN, Brno, Czech Republic) was used, equipped with appropriate SE, BSE, and EDX detectors. Microstructural images were analyzed using the ImageJ software (version 1.54f). The image processing methodology to determine the porosity of the samples involved procedures of selection, thresholding, and conversion to a W/B image, which was subsequently analyzed. The analyzed number of black area pixels relative to the total scanned area after conversion was used to express the percentage representation of porosity. Porosity calculations based on pycnometric true and volumetric bulk density were carried out using the relationship (1).

$$P_{PA} = \frac{\rho_t - \rho_b}{\rho_t}.100 \quad (1)$$

where ρ_t and ρ_b are the true and bulk densities [kg/m^3].

Pellet testing under pressure was conducted using the FP100 device (Heckert, Chemnitz, Germany) under constant loading conditions (with a vehicle displacement of 2–3 mm/min), with the maximum strength resistance until failure was evaluated. Thermodynamic modeling was performed using the "HSC Chemistry" thermodynamic software, versions 9 and 5.11, from Outokumpu Research Oy, Pori, Finland.

The reduction tests of pellet samples were conducted using modified equipment as shown in Figure 1. For the 100% hydrogen reduction, a sample of three pellets was used for each pellet type. The reduction temperatures were set at 600 °C, and an experiment with one type of pellet B was also carried out at a higher temperature (800 °C) to verify the effect of temperature on the reduction process. The temperature was set to 600 °C because

the aim of this research was to contribute to the determination of the reaction mechanism at lower temperatures.

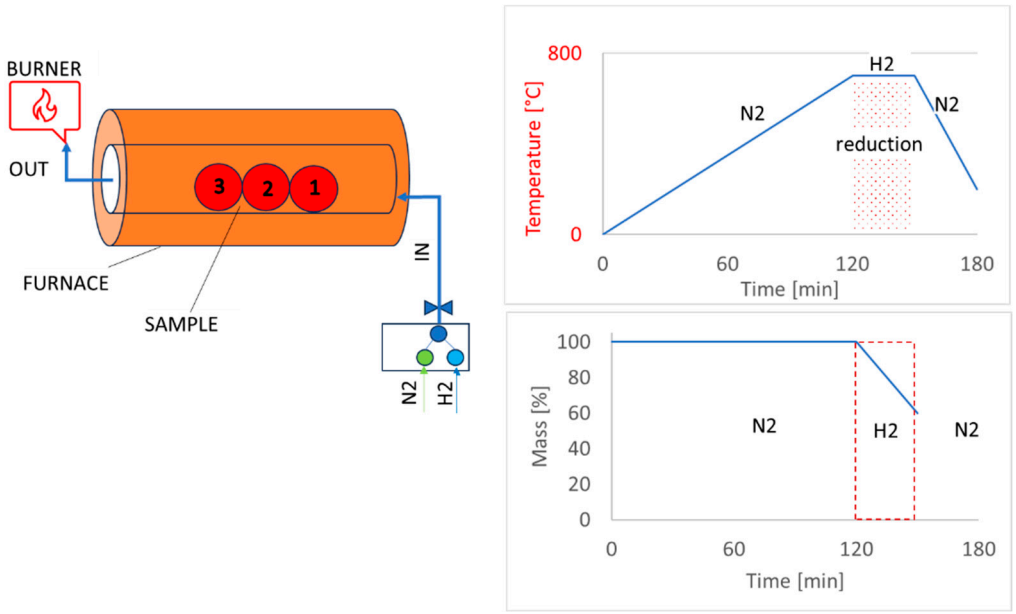

Figure 1. Schematic of the hydrogen pellet reduction experiments.

The ramp to the isothermal reduction temperature (600 °C or 800 °C) was set at a gradient of 10 °C/min in an inert N_2 atmosphere with 99.999% purity. Reduction in the 100% H_2 atmosphere was carried out at isothermal conditions for 30 min, followed by controlled cooling of the pellets in nitrogen at a gradient of 20 °C/min until ambient temperature was reached. The reduced pellet samples were then weighed to calculate the weight loss. A summary of the experiments is presented in Table 1.

The degree of reduction was expressed based on the amount of oxygen removed relative to the maximum removable oxygen from iron oxides:

$$R(\%) = \frac{(m_{O_i} - m_{O_r})}{m_{O_i}} \times 100[\%] \quad (2)$$

where

m_{Oi} is the mass of oxygen initially present in the iron oxides before reduction;
m_{Or} is the mass of oxygen remaining in the iron oxides after reduction.

Based on the apparatus shown in Figure 1, a mathematical model was developed to determine the key characteristics of the process, such as the temperature field distribution and fluid flow within the system. The model was created using Ansys 2023 R1 software.

The mathematical model employed the Reynolds-averaged Navier–Stokes (RANS) k-ε model, which is one of the most commonly used models in practical applications. Turbulence was computed using Equations (3) and (4). The turbulent kinetic energy k and its dissipation rate ϵ were derived from the corresponding transport equations [29].

$$\frac{\partial}{\partial t}(\rho k) + \frac{\partial}{\partial xj}(\rho k u_j) = \frac{\partial}{\partial x_j}\left[\left(\mu + \frac{\mu_t}{\sigma_k}\right)\frac{\partial k}{\partial x_j}\right] + G_k + G_b - \rho\varepsilon - Y_M + S_k \quad (3)$$

$$\frac{\partial}{\partial t}(\rho \varepsilon) + \frac{\partial}{\partial xj}(\rho \varepsilon u_j) = \frac{\partial}{\partial x_j}\left[\left(\mu + \frac{\mu_t}{\sigma_\varepsilon}\right)\frac{\partial \varepsilon}{\partial x_j}\right] + \rho C_1 S_\varepsilon - \rho C_2 \frac{\varepsilon^2}{k + \sqrt{v\varepsilon}} + C_{1\varepsilon}\frac{\varepsilon}{k} C_{3\varepsilon} G_b + S_\varepsilon \quad (4)$$

where the following apply:

G_k—generation of turbulence kinetic energy due to velocity gradients;

G_b—generation of the kinetic energy of turbulence due to buoyancy;
Y_M—contribution from fluctuating dilatations in compressible turbulent flow to total dissipation;
$C_{1\varepsilon}$ C_2, C_3—model constants;
σ_k, σ_ε—model constants—turbulent Prandtl numbers for k and ε (-);
S_k, S_ε—user-defined source members.
Model constants:
C2-Epsilon—1.9
TKE Prandtl number—1
TDR Prandtl number—1.2
Energy Prandtl number—0.85
Wall Prandtl number—0.85
Turbulent Schmidt number—0.7

Ansys 2023 R1 software solved the general forms of the conservation equations for mass (5), momentum (6), and energy (7) [29].

$$\frac{\partial \rho}{\partial t} + \nabla.\left(\rho \vec{v}\right) = 0 \tag{5}$$

where the following apply:

$|\rho|$ is the fluid density;
$|t|$ is time;
$\vec{v}$ is the velocity vector of the fluid.
$\nabla.(\rho \vec{v})$ represents the divergence of the mass flux (rate of mass flow per unit area).

The general form of the momentum conservation equation in the *i*-th direction is

$$\frac{\partial}{\partial t}(\rho v_i) + \nabla.\left(\rho \vec{v} v_i\right) = -\frac{\partial p}{\partial x_i} + \nabla.\tau_{ij} + \rho g_i + F_i \tag{6}$$

where the following apply:

v_i is the velocity component in the *i*-th direction;
p is the pressure;
τ_{ij} is the viscous stress tensor, representing the viscous forces acting on the fluid;
g_i represents the gravitational acceleration in the i-th direction;
F_i—is an external body force (e.g., due to electromagnetic fields or other forces).

$$\frac{\partial}{\partial t}(\rho E) + \nabla.\left(\vec{v}(\rho E + p)\right) = \nabla.(k \nabla T) + S_E \tag{7}$$

where the following apply:

E is the total energy per unit mass, which includes internal energy and kinetic energy;
T is the temperature;
k is the thermal conductivity of the fluid;
$\nabla.(k\nabla T)$ represents the heat conduction (Fourier's law);
S_E represents energy sources (e.g., due to chemical reactions, radiation, or other heat sources).

3. Results and Discussion

The chemical, physical, physicochemical, metallurgical, and mechanical properties of the pellets based on material research are summarized in Table 2.

Table 2. Summary of the physicochemical properties of Fe pellets.

Iron Ore Pellets		**A** 	**B** 	**C** 	**D** 
Chemical composition (wt %)	Fe_{TOT}	67.34	65.32	65.04	65.42
	FeO	0.43	2.16	0.43	0.86
	SiO_2	2.6	2.673	5.18	5.04
	Al_2O_3	0.20.1	0.446	0.279	0.158
	CaO	0.30	1.43	0.191	0.313
	MgO	-	1.213	0.786	-
	P	0.041	0.039	0.042	0.04
	S	0.014	0.019	0.016	0.02
	K_2O	0.133	0.155	0.16	0.25
	Others *	29.37	30.40	30.97	30.53
Granulometric composition (%)	<10 mm	8.72	0	33.91	6.73
	>10 mm	91.28	100	66.09	93.27
	>16 mm	2.06	5.13	2.01	2.00
D_{avg} (mm)		12.04	13.49	10.56	12.24
Apparent specific density ($kg \cdot m^{-3}$)	ρ_A	2253	2158	2150	2080
True specific density ($kg \cdot m^{-3}$)	ρ_t	4788	4750	4606	4624
Volumetric (bulk) specific density ($kg \cdot m^{-3}$)	ρ_b	4067	3510	3639	3762
Porosity— pycnometric analysis (%)	P_{PA}	15.06	26.09	20.99	18.83
Porosity— microscopic analysis (%)	P_{MAO}	2.53	9.19	6.86	5.13
Compressive strength (N/pellet)	Mean value	2255	2308	1898	2033
Melting point (°C)		-	-	1505	1499
Mineralogical composition	XRD	Hematite Magnetite Quartz Cristobalite	Hematite Magnetite Quartz	Hematite Magnetite Quartz Cristobalite	Hematite Magnetite Quartz Cristobalite

Others * = primarily an analysis of oxygen and hydrogen in Fe phases.

3.1. Physicochemical Properties of the Studied Pellets

The first of the evaluated properties of the pellets was their chemical composition. The supplied samples were subjected to XRF analysis of their chemical composition. The results indicate that the richest pellets are Pellet A, with a total iron content (Fe_{TOT}) of 67.34%. In contrast, the poorest pellets are Pellet C, with a total iron content of 65.04%. Fluxed pellets labeled as B naturally had the highest basicity due to the increased content

of CaO. Pellets D and C have very similar compositions, as well as the highest content of SiO_2. Fluctuations in the FeO content suggest a theoretical difference in the reducibility of the pellets, where the degree of reduction will be inversely proportional to the FeO content at the input.

The values of bulk density, apparent density, and true density were determined for all types of Fe pellets, with their average values correlating with the declared grade (Table 2). Sieve analysis of the pellets was performed to determine the granulometry and average particle size. From the comparison of the sieve analysis, it can be seen that the average particle size (D_{avg}) of the pellets ranges from 10 to 13.5 mm, with Pellet C showing an increased fraction of material below 10 mm. The results of the density measurements reflect the condition and nature of the samples. The true density of the final pellets depends on their chemical and phase composition. Logically, this value should increase with the pellet's grade. Pellet A, with the highest Fe_{TOT} content, has the highest true density. For the other pellets, with relatively similar grades, the arrangement density and the proportion of different phases with their specific densities play a role. In the case of bulk densities, in addition to the aforementioned factors, the granulometry of the pellets and their porosity also play a role.

Using a high-temperature microscope, the surface and volume changes of the analyzed samples were observed during heating up to 1500 °C to determine the melting temperatures (Figure 2). High-temperature analysis of Pellets A, B, C, and D in an air atmosphere revealed that Pellets A and B did not melt, although they exhibited volume changes and deformation at temperatures around 1500 °C. In contrast, Pellet D began to melt at temperatures between 1470–1505 °C, and Pellet C at 1460–1499 °C. The results show that Pellets D and C have lower melting temperatures, while Pellets A and B demonstrate greater stability at higher temperatures. Pellet A demonstrated the highest thermal stability, with only deformation occurring at the maximum heating temperature (1500 °C). In contrast, Pellet C exhibited the lowest stability, with a total transition range from 1440 to 1499 °C. From a chemical standpoint, Pellet A has the highest enrichment, while its SiO_2, Al_2O_3, and K_2O contents are lower. Pellets C and D have very similar chemical compositions, which is reflected in their comparable thermal stability. Pellet B is essentially a fluxed version of Pellet A, produced with added lime, resulting in slightly lower stability compared to Pellet A. This is likely due to the presence of calcium silicate ferrites, which generally have a lower melting point than hematite and magnetite phases. On the other hand, thermal stability can also be reduced by the presence of Fe silicate phases (such as fayalite). Although these were not detected by XRD analysis, microstructural analysis confirmed their presence. This is further supported by their expected formation during the firing process of pellets with higher SiO_2 content. Pellets C and D contained a significantly higher SiO_2 content, part of which formed complex compounds with iron oxide type of iron silicates, e.g., fayalite Fe_2SiO_4 with a lower melting point than the individual oxides, hematite and magnetite, and calcium silicates. A higher proportion of these iron silicates in Pellets C and D was also detected during microscopic observation of the pellet microstructure (Figure 3).

The XRD analysis of the tested pellets, in contrast with certified chemical analysis, indicates that the methodology was able to identify the major phases of iron oxides, namely hematite and magnetite, as well as SiO_2 phases (quartz and cristobalite). Minor phases based on complex iron oxide compounds, CaO, and SiO_2 (ferrites and silicates) were not identified due to their low detection limit. Some insight into the presence of individual phases was provided by the microstructural SEM EDX analysis.

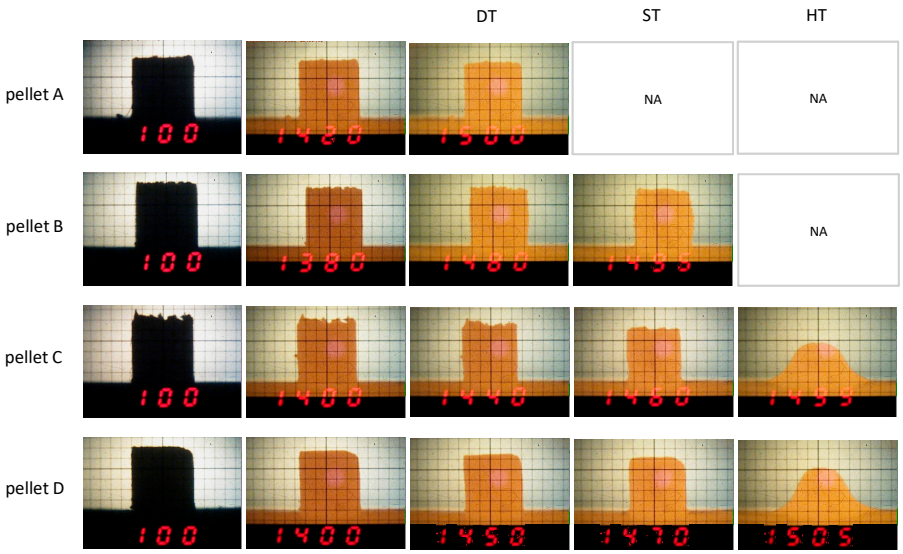

Figure 2. High-temperature observation of iron pellet samples. DT = deformation temperature (°C); ST = shrinkage temperature (°C); HT = hemisphere temperature or melting point (°C); NA—not analyzed at higher temperatures due to the temperature limit being reached, with a maximum of about 1515 °C.

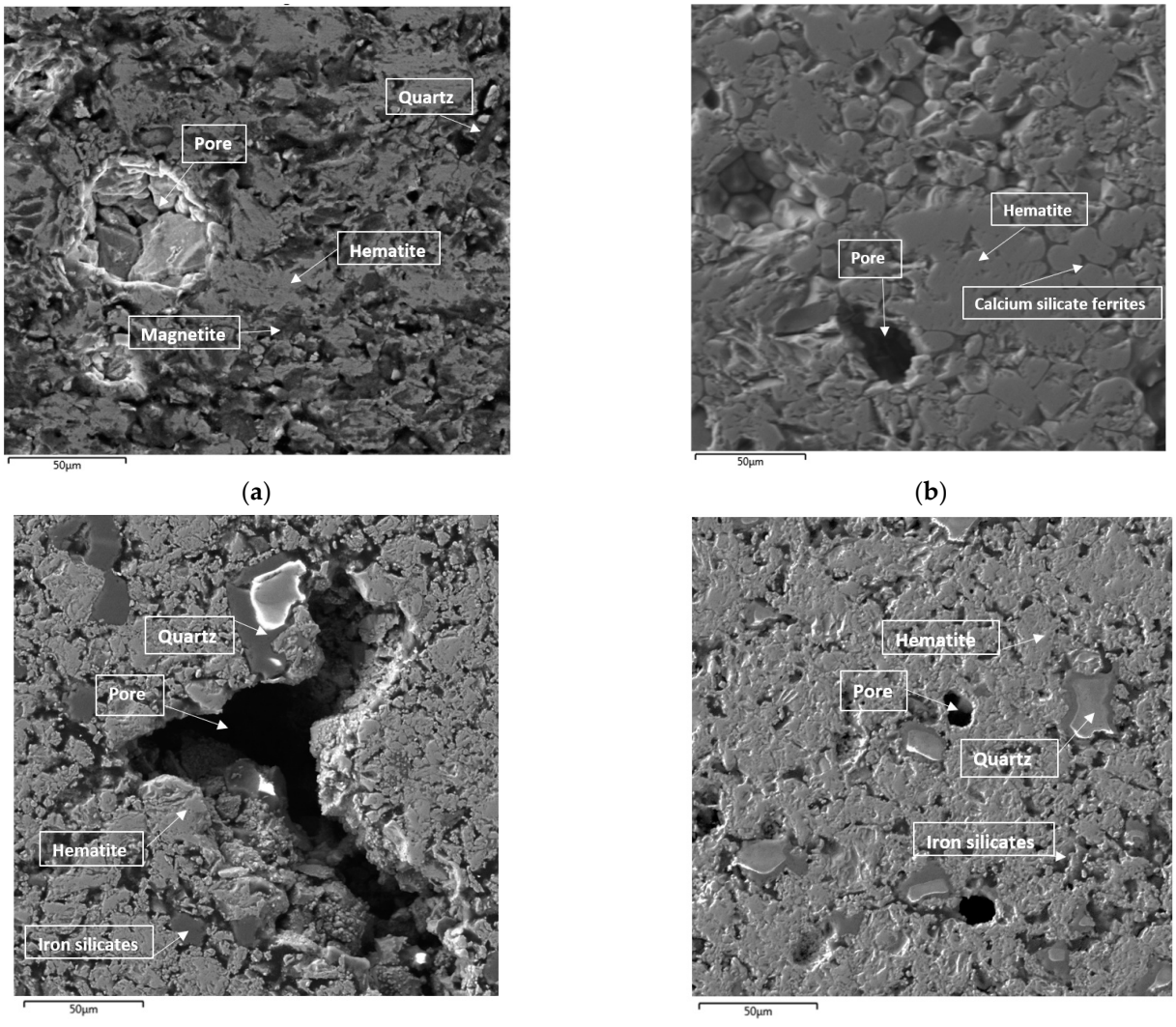

Figure 3. Microstructures of the Fe pellet samples: (**a**) A; (**b**) B; (**c**) C; (**d**) D.

Microscopic observation of the samples was performed on all analyzed pellets. Microstructural evaluation is important for determining and mapping the distribution of individual mineralogical phases and monitoring the homogeneity of the scanned areas. EDX analysis proved to be a useful tool for determining the phase composition of the pellets. From the comparison and analyses, we can observe certain differences in the phase composition, as well as differences in the homogeneity and porosity of the analyzed pellets. The phases identified via EDX in individual pellet types were found to be homogeneously distributed in samples A, C, and D (Table 3, Figure 3). The fluxed Pellet B showed slight inhomogeneity in distribution.

Table 3. Identified phase composition of the studied Fe pellets based on microscopic analysis.

Pellet Name	Pellet A	Pellet B	Pellet C	Pellet D
Identified phases	Hematite	Hematite	Hematite	Hematite
	Magnetite	Calcium silicate ferrites + calcium silicates	Iron silicates	Iron silicates + complexes
	Quartz	Quartz	Quartz	Quartz
Sample homogeneity	Homogeneous samples	Slight inhomogeneity of the samples	Homogeneous samples	Homogeneous samples

SEM EDX analysis revealed that the pellets are predominantly based on hematite, with other typical phases detected. In Pellet A, magnetite was also observed. Fluxed Pellet B contains calcium silicate ferrites and calcium silicates. Pellet C, in addition to hematite and quartz, contains iron silicates, while Pellet D contains, along with iron silicates, phases based on various complex compounds, for example, hedenbergite $CaFe(SiO_3)_2$. Point spectral EDX analyses confirmed the presence of individual phases typical for oxide pellets. This methodology confirmed the presence of phases that were not recorded by conventional XRD analysis, likely due to the detection limit of X-ray diffraction.

Microstructural images were subjected to image analysis using ImageJ software version 1.54f. The goal was to use this software tool to determine whether there is a correlation between the porosity determined from the microstructural images and the porosity of the actual pellets, as measured through pycnometric and volumetric true density calculations.

The results of the porosity determination using the pellet microstructure and pycnometric analysis are presented in Table 2 and Figure 4.

In measuring the porosity of samples A, B, C, and D, two different methodologies were used: computational and microscopic analysis, with each method providing a different perspective on the material's structure and its porosity. The computational porosity methodology is based on the differences in the measured densities. It is expressed as the ratio of the difference between the true density and bulk density to the true density. The computational methodology shows the highest porosity for sample B (26.09%), meaning that this material has the most internal pores. In contrast, Pellet A has the lowest porosity (15.06%), indicating that this material has fewer internal pores. Microscopic analysis involves observing the sample under a microscope. This method allows for direct measurement and assessment of the internal pores in the cross-section of the pellet. In microscopic analysis, the pores intersected by the cross-section are internal pores. The result is the percentage of pores directly observable in the microscopic images. Microscopic analysis revealed that sample B also has the highest visible porosity (9.19%), while sample A shows the lowest porosity (2.53%).

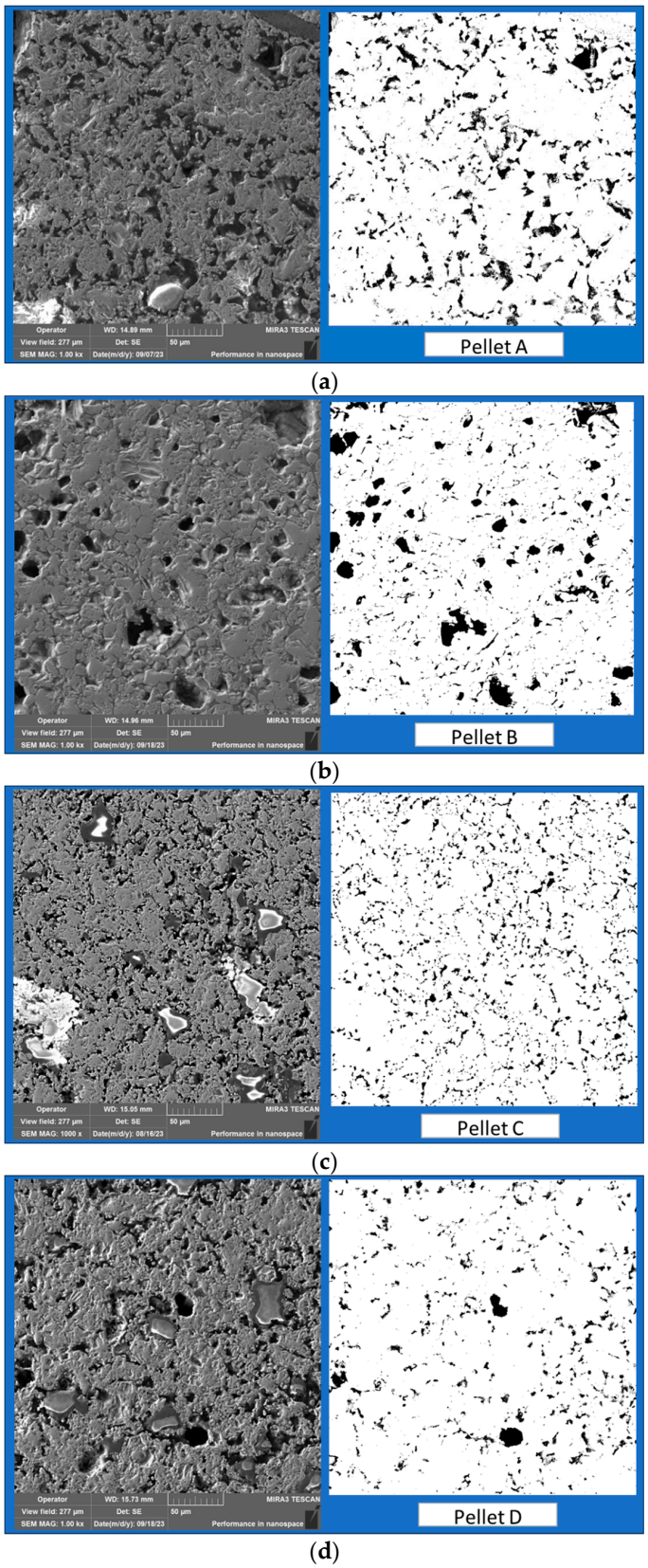

Figure 4. Image conversion of the microstructural images for porosity assessment (black areas on the image to the right). (**a**) Pellet A; (**b**) Pellet B; (**c**) Pellet C; (**d**) Pellet D.

The analysis of porosity in the microstructure also shows differences in pore size and the homogeneity of pore distribution. The largest pores were observed in sample B, while the highest homogeneity of pore distribution was found in sample C. Figure 5 illustrates

the correlation between porosity determined from microstructural images and the porosity of the actual pellets determined using computational methods based on pycnometric and volumetric true density. It was found that both methodologies for determining this key property for pellet reduction are closely correlated, as shown in Table 2 and Figure 5. The porosity of the pellets depends on the quantity and physicochemical properties of the melt that forms during high-temperature sintering of the pellets. The reasons why the computational and microscopic porosities do not agree are that the porosity is non-uniform (which is obvious from Figure 6) and/or the image analysis used to derive porosity from a cross-sectional micrograph is limited due to the relative volume of the pellet analyzed. The computational porosity is derived from the whole of the pellet, while the microscopic porosity is derived from a small area of the cross-section.

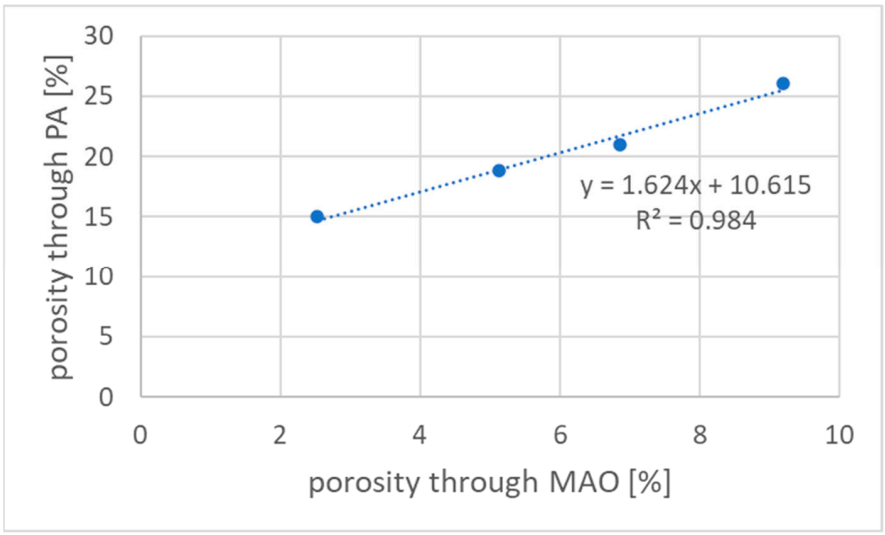

Figure 5. Correlation of pellet porosities. MAO—porosity based on microstructure; PA—calculation based on pycnometric and volumetric true density.

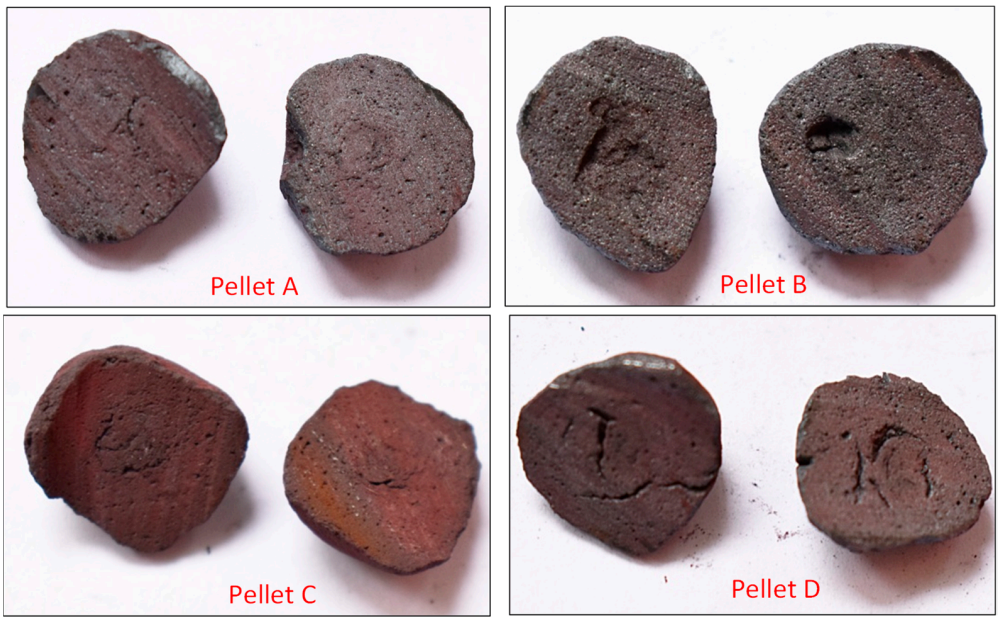

Figure 6. Cross-sections of the analyzed pellets.

Figure 6 shows cross-sections of four types of iron pellets (A, B, C, D), highlighting differences in their macrostructure and crack formation. Pellet A exhibits a homogeneous

and fine-grained structure with minimal cracks and pores. In contrast, Pellet B has a less homogeneous structure with larger pores. Pellet D shows the presence of larger cracks and irregularities, which could negatively affect its mechanical stability during reduction.

Figure 7 presents the compressive strengths of the pellets, showing that Pellet A has the highest average strength with a minimal range of measured strengths, whereas Pellet B exhibits a wide range of strengths, indicating a less homogeneous structure.

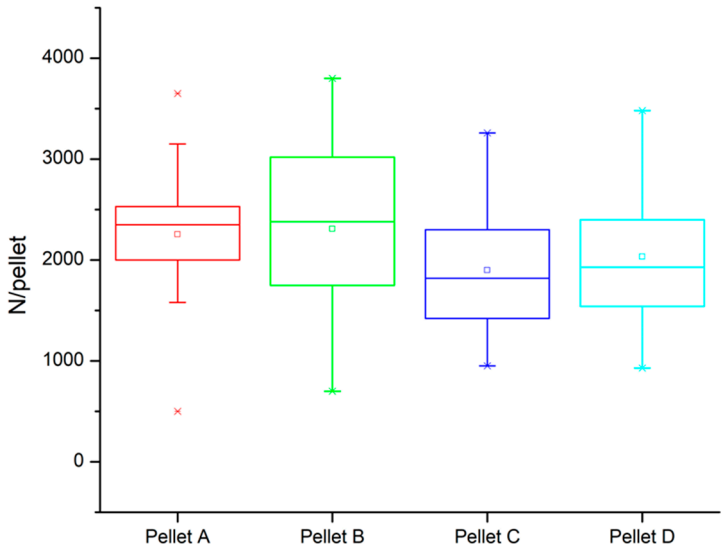

Figure 7. Mechanical properties of Fe pellets under compression.

3.2. Thermodynamic Analysis of the Prediction of Pellet Reduction in an H_2 Atmosphere

The design of the experimental methodology focused on the reduction potential of pellets and their behavior under defined conditions and was based, among other factors, on the results of predictive models obtained using the thermodynamic software HSC Chemistry 9. The computational modules used were Reaction Equations (Rea), Equilibrium Compositions (Gem), and Heat and Material Balances (Bal).

The reduction of the tested pellets, simulated under different ratios and amounts of reducing gases, was carried out based on the modeling of the reaction system. The prediction of pellet reduction for simulated conditions in an H_2 atmosphere at a constant temperature was conducted based on the input chemical composition of the pellets and the stoichiometric calculation of their predicted mineralogical composition.

For the study of reduction conditions, the basic assumptions of the Fe-O-H system under H_2–H_2O conditions were used. For this purpose, a Baur–Glessner diagram (Figure 8) was constructed based on the thermodynamic data from HSC Chemistry. Figure 8 compares the carbothermic and hydrogen reduction of iron oxides.

The BG diagram of the equilibrium composition for the Fe-O-C and Fe-O-H systems shows the stability regions of individual phases for the given atmospheric conditions and temperature range. At points A and A′ (triple points), the phases of magnetite, wüstite, and metallic iron coexist in equilibrium for the respective systems. The Boudouard line is included in the diagram as part of the system, as this reversible reaction occurs during reduction, for example, in a blast furnace, which can lead to the formation of so-called soot-like carbon. In addition to the Boudouard line, the reaction between carbon monoxide and hydrogen is also indicated, resulting in carbon and water vapor. This reaction, in terms of soot-like carbon, proceeds up to a threshold temperature of about 670 °C. Above this temperature, the reaction starts to proceed in the reverse direction.

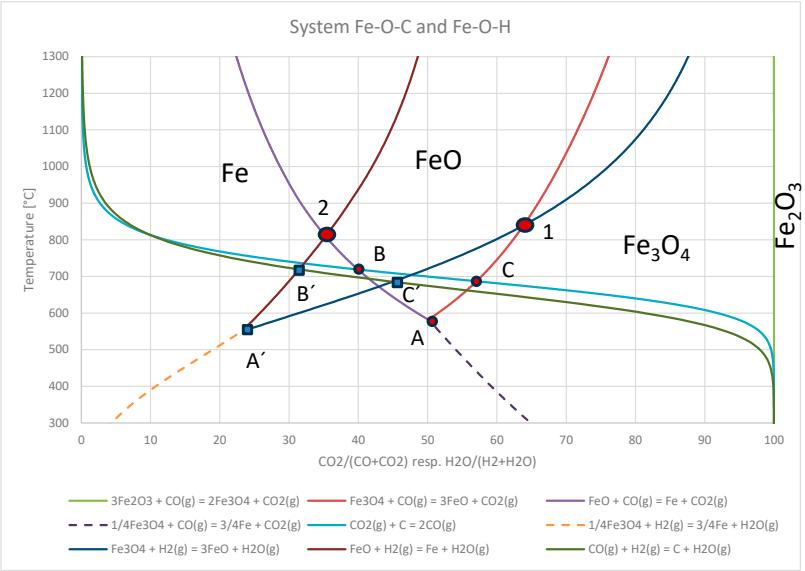

Figure 8. Baur–Glessner diagram with the Boudouard reaction (BR) and the CO and H_2 reactions.

For hydrogen reduction, the boundary line of the equilibrium reaction between CO and H_2, resulting in CO_2 and H_2O, applies. The dashed areas of the systems indicate the equilibrium transitions from magnetite directly to iron. In these temperature intervals (below approximately 570 °C), wüstite is unstable and decomposes into magnetite and iron. It is observed that for the transition from magnetite to metallic iron in the temperature range below 570 °C, a hydrogen atmosphere of 80–100% H_2 and 0–20% H_2O is required.

Thermodynamic calculations and the graph indicate that CO has a higher reduction potential than hydrogen at lower temperatures, whereas, at higher temperatures, hydrogen reduction is more stable. The intersections of both systems (points 1 and 2) represent areas with the same reduction potential for CO and H_2. It should be noted that the kinetics of the reduction processes are proportional to temperature, and therefore, low-temperature reductions take much longer. From a kinetic perspective, hydrogen, due to its size and high diffusion ability, is a faster reducer compared to CO at temperatures above 850 °C.

The reduction of hematite (Fe_2O_3) to iron (Fe) using hydrogen occurs in several consecutive steps, each taking place at different temperatures and either consuming or releasing energy. Initially, hematite is reduced to magnetite (Fe_3O_4), and then, at temperatures above 570 °C, it further reduces to wüstite (FeO). Below 570 °C, magnetite is directly reduced to iron because wüstite is unstable under these conditions. A detailed understanding of these reactions is key to optimizing reduction conditions in metallurgical processes that use hydrogen for iron production.

$$3Fe_2O_3 + H_{2(g)} \rightarrow 2Fe_3O_4 + H_2O_{(g)} \qquad \Delta H^o = -3.197\ \text{kJ/mol} \tag{8}$$

$$Fe_3O_4 + 2H_{2(g)} \rightarrow 3Fe + 4H_2O_{(g)} \qquad T < 570\ ^\circ\text{C} \qquad \Delta H^o = 151.079\ \text{kJ/mol} \tag{9}$$

$$Fe_3O_4 + H_{2(g)} \rightarrow 3FeO + H_2O_{(g)} \qquad T > 570\ ^\circ\text{C} \qquad \Delta H^o = 74.747\ \text{kJ/mol} \tag{10}$$

$$FeO + H_{2(g)} \rightarrow Fe + H_2O_{(g)} \qquad T < 570\ ^\circ\text{C} \qquad \Delta H^o = 25.444\ \text{kJ/mol} \tag{11}$$

These reactions, (8)–(11), are crucial for thermodynamic studies in the HSC program, as they enable the optimization of temperature conditions and the analysis of energy requirements during the reduction of hematite to iron [30]. HSC models thermal changes, allowing the determination of ideal conditions for efficient reduction and evaluating the stability of intermediates such as magnetite and wüstite.

Based on the aforementioned reactions, thermodynamic models for iron ore pellets have been developed, allowing for a detailed analysis of the reduction processes under various temperature conditions.

Hematite is reduced to magnetite very quickly and easily, and magnetite preferentially transitions to Fe at lower temperatures, where FeO is unstable and decomposes into Fe_3O_4 and Fe. As the temperature increases, not only does the proportion of reduced Fe increase but also the proportion of wüstite, which slowly reduces from 400 °C onward, leading to an increase in Fe. Differences in the reduction processes can be observed based on the content of the individual components of the system (Figure 9).

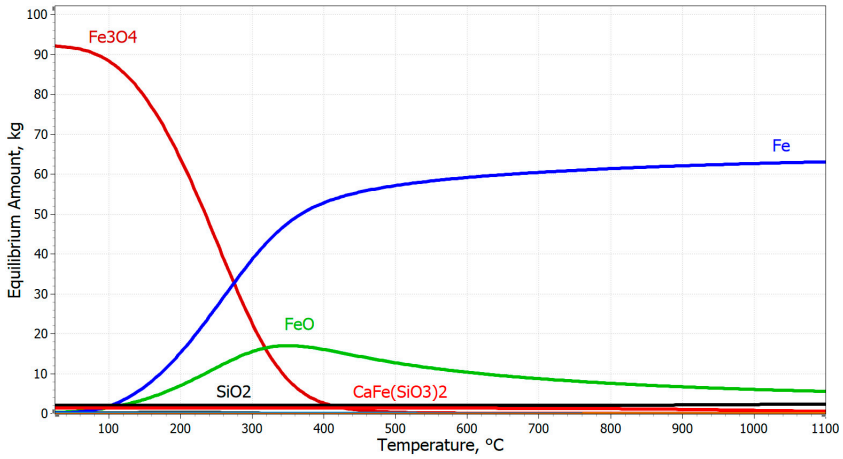

(**a**)

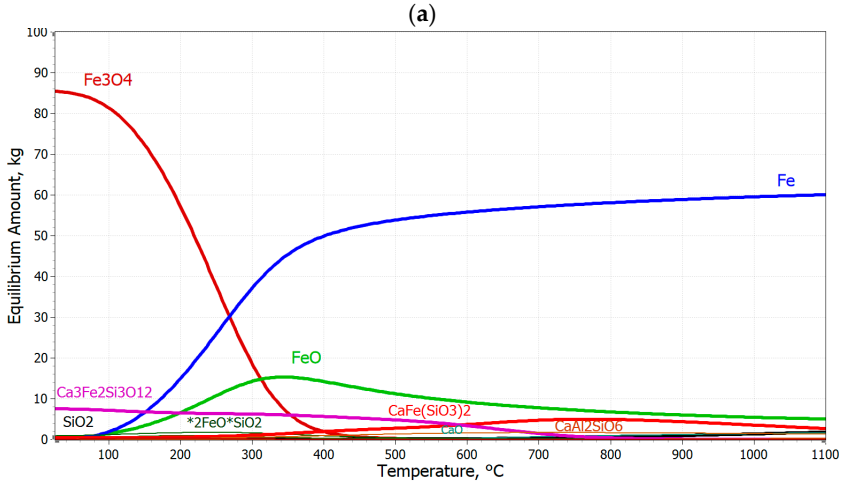

(**b**)

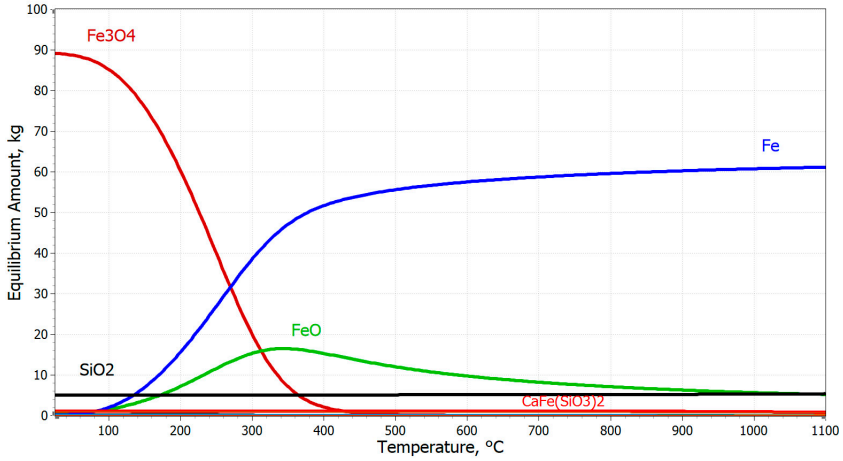

(**c**)

Figure 9. *Cont.*

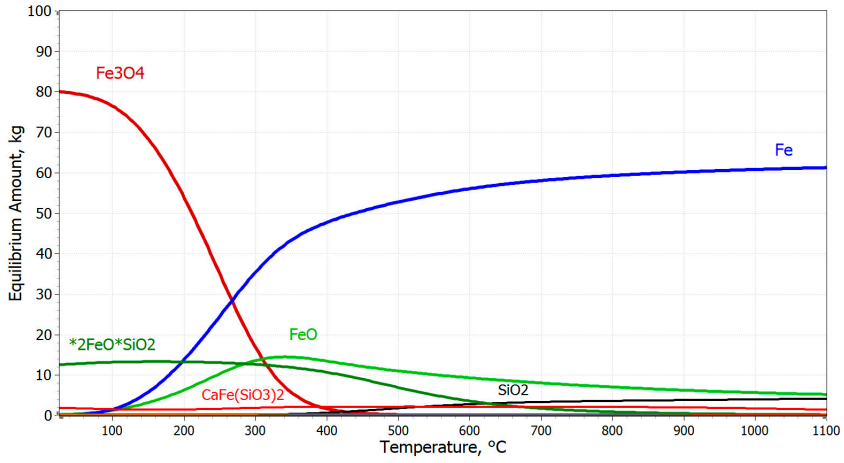

(**d**)

Figure 9. Equilibrium system of hydrogen reduction for Fe pellets: (**a**) A; (**b**) B; (**c**) C; (**d**) D. Explanation: *2FeO*SiO_2—standardized notation of a complex compound fayalite (2FeO·SiO_2) in the HSC Chemistry thermodynamic program.

When comparing simulations focused on the yield of Fe, the order of reducibility of the pellets is clearly visible (Figure 10). Thermodynamic conditions predict that in the case of a hydrogen atmosphere, Pellets D and B will perform the worst at lower temperatures; however, as the temperature increases, this deficit disappears for Pellet D, and the pellets will perform very well in this temperature range. The HSC predictions clearly indicate that the best results should be achieved with Pellet A, while the worst results among the compared pellets will be observed with the fluxed Pellet B.

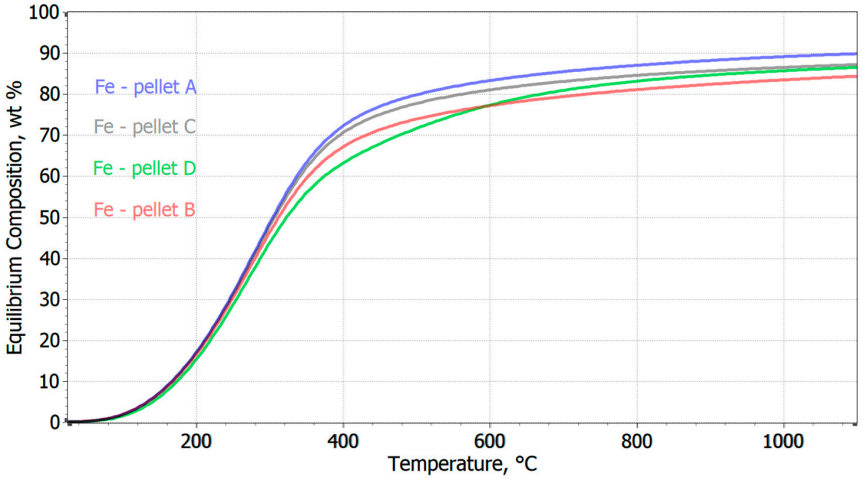

Figure 10. Predicted yield during the reduction of pellets in an H_2 atmosphere.

One of the reasons for achieving the lowest Fe yields and the more difficult reduction of Pellet B is its chemical composition, where the influence of CaO content is reflected in the proportion of individual mineralogical phases (Figure 11). At lower CaO contents (approximately up to 3.8 wt.%), the dominant phase based on CaO is calcium silicate ferrites ($CaFe(SiO_3)_2$), while at higher CaO contents, the dominant CaO-based phase is calcium ferrite ($CaO*Fe_2O_3$), which is more easily reducible. Our tested Pellet B has an average CaO content of 2.3%, where the dominant phase is the less reducible calcium silicate ferrite. Therefore, a higher reducibility of Pellet B can be expected at higher CaO contents.

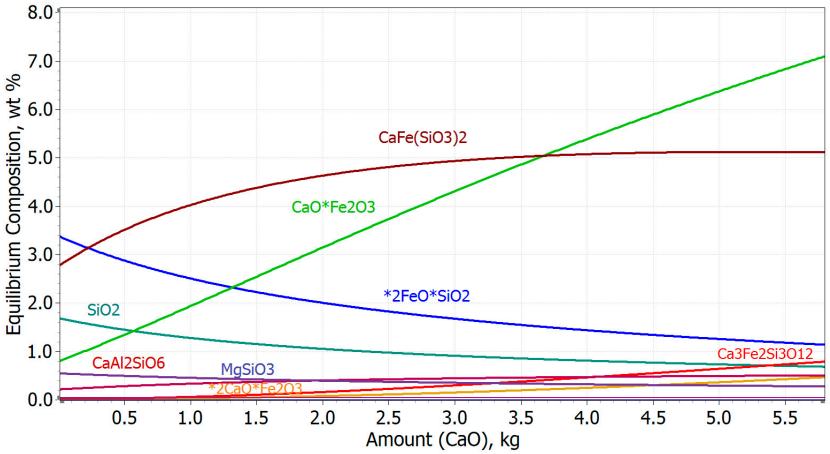

Figure 11. Equilibrium composition of calcium silicates with varying CaO content. Explanation: *2CaO*Fe_2O_3—standardized notation of a complex dicalcium ferrite (2CaO·Fe_2O_3) in the HSC Chemistry thermodynamic program.

The equilibrium amount of the pellets changes under isothermal conditions with the amount of reducing agent, and the reduction process follows a logarithmic or power-law character, as shown in Figure 12c,d. In order to confirm the correctness of the thermodynamic simulations of the equilibria for the tested pellets, the equilibria for the reduction of pure hematite were simulated (Figure 12a,b), and these were compared with the stoichiometric calculation of the considered reduction of Fe_2O_3 in three steps to obtain iron.

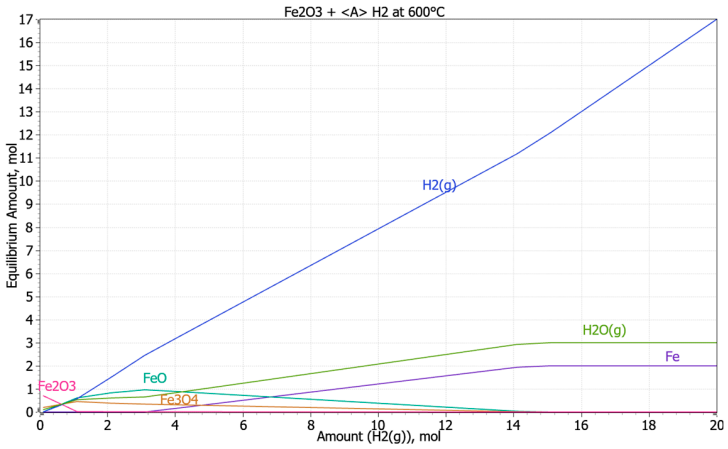

(**a**)

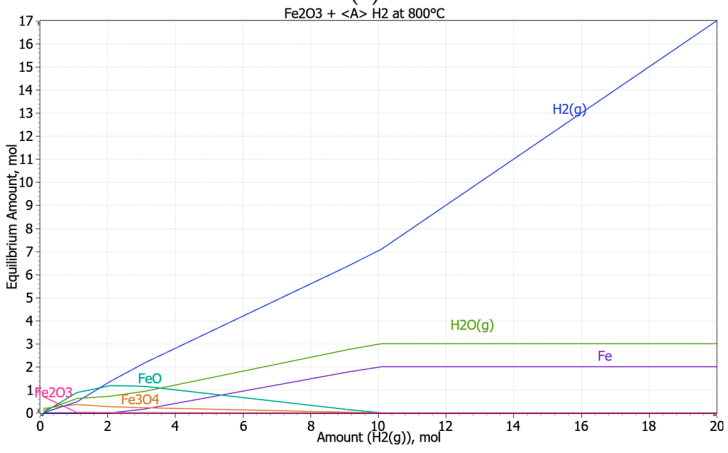

(**b**)

Figure 12. *Cont.*

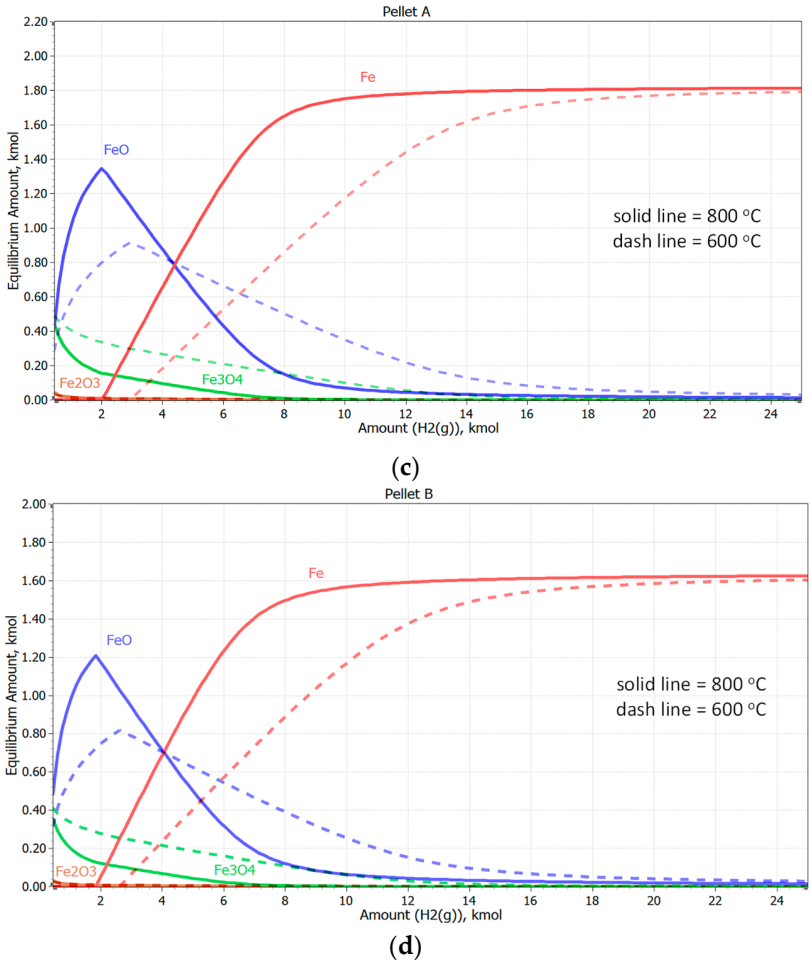

Figure 12. Comparison of Fe yield for the pure hematite and tested pellets in an H_2 atmosphere with respect to the reducing agent ratio and reduction temperature: (**a**) pure hematite at 600 °C; (**b**) pure hematite at 800 °C; (**c**) Pellet A; (**d**) Pellet B.

From Figure 12a,b, we see at first glance that for the reduction of 1 mole of Fe_2O_3 approximately 10 moles of H_2 are required at 800 °C or approximately 14 moles of H_2 at 600 °C. From the stoichiometric calculation of partial Equations (12)–(14) or their summary Equation (15), it follows that 3 moles or 67.2 L of H_2 are consumed per 1 mole of Fe_2O_3. The calculated moles may initially appear to be in contradiction with the predicted graphs (Figure 12a,b). In fact, it is necessary to take into account the displayed line of hydrogen content in the graphs (blue curve "H_2(g)") and in the relevant section subtract it from the predicted H_2 consumption, which is shown on the *x*-axis. In this way, not only is the correct consumption of the reducing agent determined, but also the exact equilibrium amounts of the components. For example, for the perpendicular section in Figure 12a on the *x*-axis at a value of 14 moles of H_2, the value of the curve "H_2(g)" is 11 moles, which gives the actual consumption of 14 − 11 = 3 moles. The intersections of the above perpendicular with the other lines further indicate the amount of Fe = 2 moles and H_2O(g) = 3 moles, which corresponds to the state of completion of the reduction of 1 mole of hematite.

$$Fe_2O_3 + 1/3H_{2(g)} \rightarrow 2/3Fe_3O_4 + 1/3H_2O_{(g)} \quad (12)$$

$$2/3Fe_3O_4 + 2/3H_{2(g)} \rightarrow 2FeO + 2/3H_2O_{(g)} \quad (13)$$

$$2FeO + 2H_{2(g)} \rightarrow 2Fe + 2H_2O_{(g)} \quad (14)$$

$$Fe_2O_3 + 3H_{2(g)} \rightarrow 2Fe + 3H_2O_{(g)} \quad (15)$$

For example, in a perpendicular section at the value of 5 moles of H_2 in Figure 12a, the actual consumption is 5 − 3.5 = 1.5 moles of H_2, so the equation would look like the following:

$$Fe_2O_3 + 1.5H_{2(g)} \rightarrow 0.2Fe_3O_4 + 0.8FeO + 0.6Fe + 1.5H_2O_{(g)} \quad (16)$$

We observe the same differences in the so-called yield of reduced iron across the entire range of reducing agents for the individual pellet types (see Figure 12c,d). The observed differences in equilibrium composition are up to 10 wt.% within the compared commodities. The maximum Fe yield in Pellet A in an H_2 atmosphere at 800 °C is 94% (at 600 °C, it is 93%). For Pellet B, the predicted Fe yield is 85% at 600 °C and 87% at 800 °C. The increase in temperature supports the reduction process, leading to a higher yield of metallic Fe.

3.3. Reduction of Pellets in 100% H_2 Atmosphere

Reduction tests of pellet samples were carried out using modified equipment as shown in Figure 1.

Both graphs (Figure 13) illustrate the dependence of the reduction degree of iron pellets on time during a 100% hydrogen reduction under different conditions.

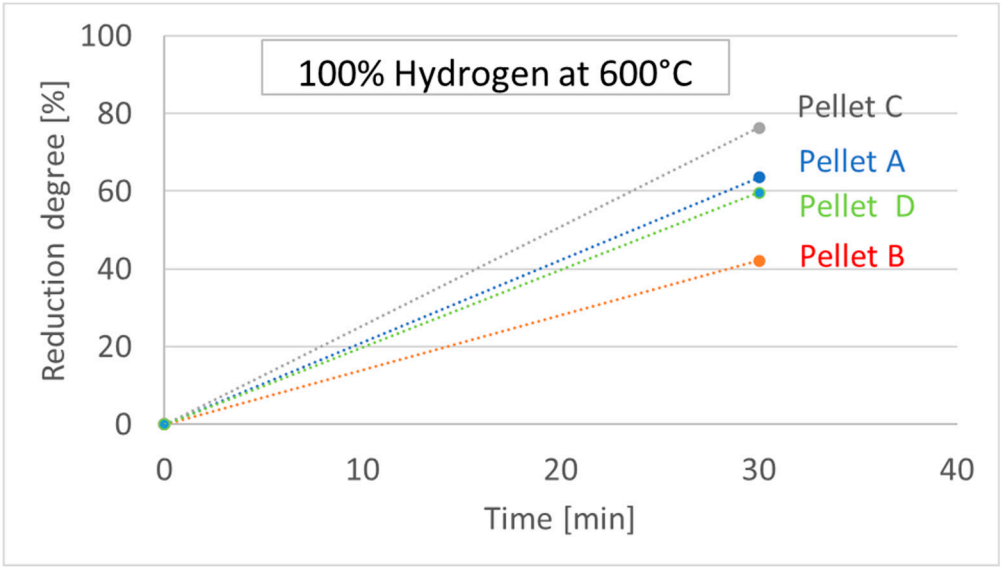

(**a**)

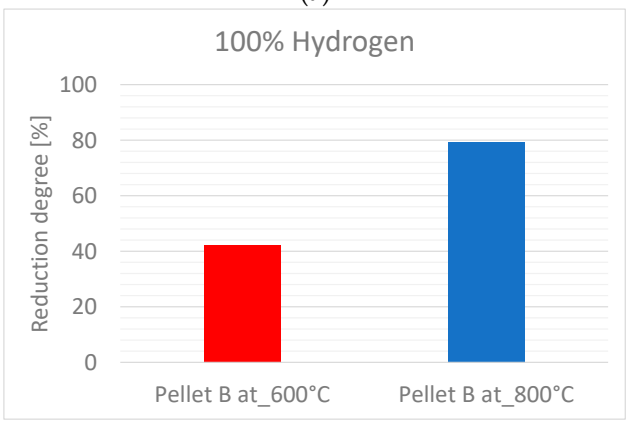

(**b**)

Figure 13. Hydrogen reduction indexes of pellets and the effect of temperature on the reduction degree: (**a**) 600 °C; (**b**) 800 °C.

The upper graph (Figure 13a) shows the experimental results at 600 °C for four different pellet types: A, B, C, and D. Over the course of 30 min, samples C and A achieve the highest reduction degree, approximately 80%, indicating their better reducibility at this temperature. On the other hand, sample B shows a significantly lower reduction, around 50% after the same time, suggesting that this fluxed sample has a lower reduction capacity under these conditions.

The lower graph (Figure 13b) compares the reducibility of sample B at two temperatures: 600 °C and 800 °C. While at 600 °C, the sample reaches a reduction degree of about 50% after 30 min, at 800 °C, it reaches almost 80%. This significant difference shows that higher temperature greatly improves the speed and efficiency of hydrogen reduction.

The results (Figure 13) generally correlate with the thermodynamic models and simulations (Figure 14), except for Pellet C, which in practical tests in a hydrogen atmosphere demonstrated better reducibility than the predicted favored Pellet A. This discrepancy suggests the presence of additional factors not included in the thermodynamic calculations, which significantly affect the reduction process. These parameters must therefore be considered in a comprehensive evaluation of the reduction potential of the pellets. One reason for the better reducibility of Pellet C compared to Pellet A may be its higher porosity and more homogeneous pore distribution in Pellet C.

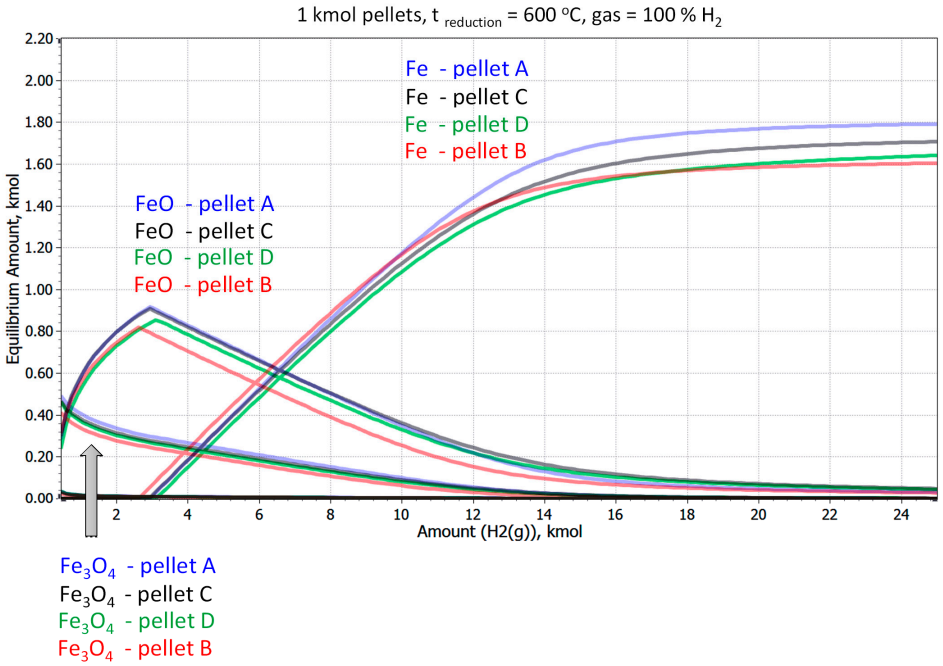

Figure 14. Comparison of Fe yield for the tested pellets in an H_2 atmosphere—thermodynamic simulation.

The prediction results confirm the positive impact of these parameters and predict the required amounts of the reducing agent to achieve maximum yield. At lower temperatures, significantly higher amounts of the reducing agent are needed to achieve the same reduction effect, meaning its utilization for reduction work is lower.

The results of the mathematical model, presented in Figure 15, illustrate the changes in the temperature field of the gas atmosphere in the heating zone of the ceramic tube, where the samples were placed during reduction at an isothermal temperature. The flow simulation focused only on the isothermal reduction phase and simulated the change in temperature of the gas phase flowing through the system. Figure 15 clearly shows that the flow of the reducing agent (H_2) affects the temperature distribution near the pellets, cooling the area around the first pellet.

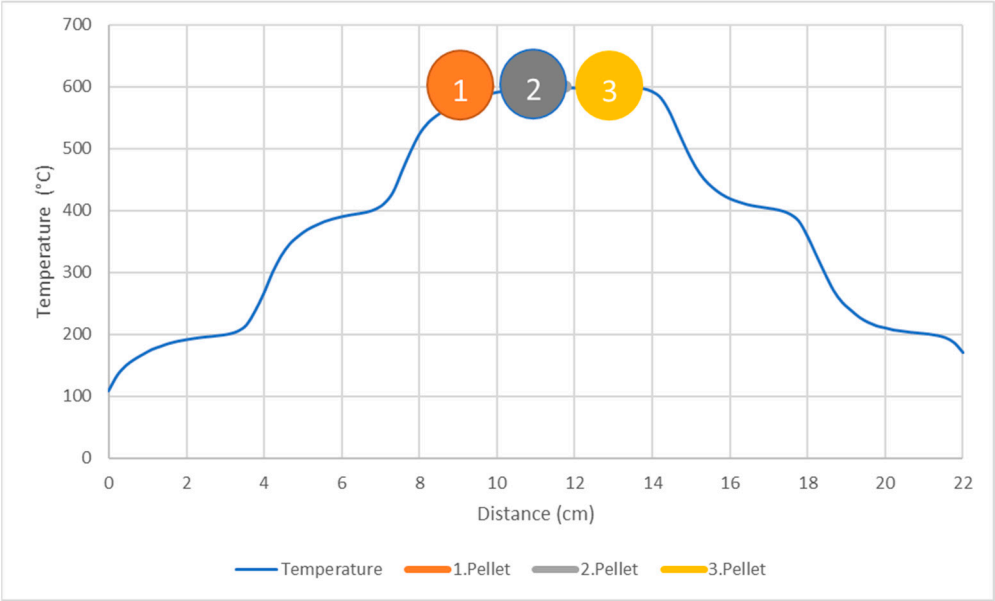

Figure 15. Temperature profile in the ceramic tube during hydrogen reduction (H_2 input from the left).

Figure 16 illustrates the uneven temperature distribution on the surface of the pellets. Since the kinetics of chemical reactions are significantly influenced by temperature, this uneven temperature distribution contributes to the lower reduction levels observed in the process.

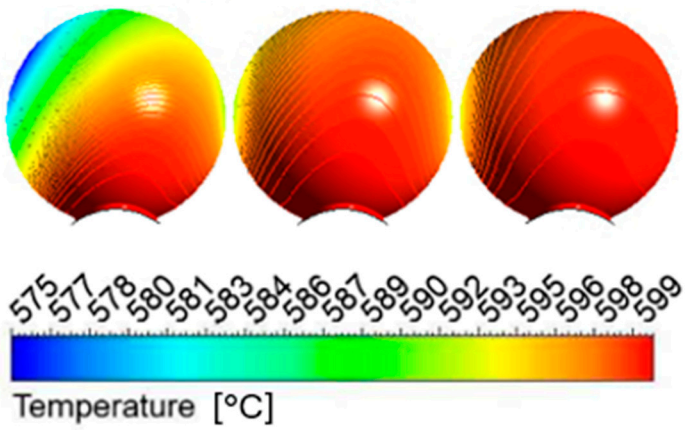

Figure 16. Graphical representation of the temperature distribution on the analyzed sample.

Figure 17 illustrates the distribution of the velocity field in the system. Due to the gas flow moving from the warmer zones to the cooler ones, accompanied by a change in gas density, vortex zones form behind the pellets. The turbulent area behind the three pellets can also affect the reduction effect, as it influences the residence time of the reactants and increases the diffusion of the reacting components.

As part of the analysis, differences in reduction were also recorded and confirmed for the individual pellets placed in the furnace (pellets 1, 2, and 3) during hydrogen exposure (Figure 18). These differences confirm the effect of the reducing gas flow through the layer, which needs to be taken into account.

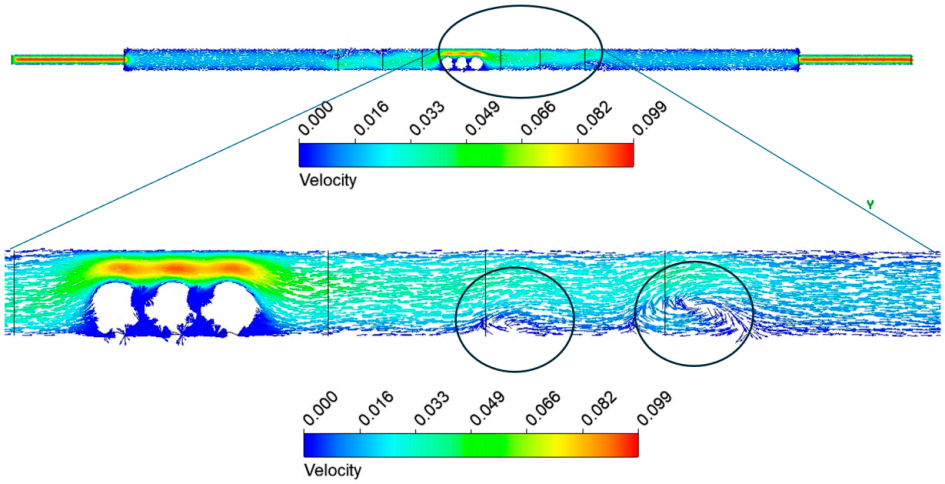

Figure 17. Flow simulation in the tube.

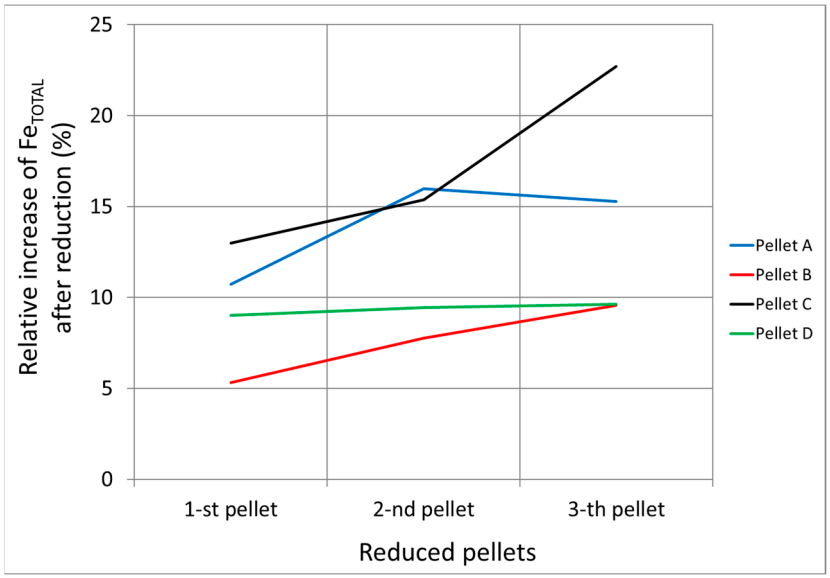

Figure 18. Comparison of the change in % FeTOT in the pellets after reduction in the H_2 experiments.

From the visual observation of the pellets (Table 4), we can track the macrostructure of the pellets, cracking, as well as various volumes within the diffusion mechanism of the reduction. The strength characteristics of the pellets after reduction were significantly reduced, which was evident during their division, where partial breakdown occurred. This reduced strength corresponds to the structural changes during the reduction, increased porosity, and weakening of the bonds due to phase transformations. Pellet A maintained its integrity, but the presence of surface cracks suggests internal changes in the material during reduction. After manual division, significant porosity and a layered structure were revealed, indicating oxygen loss during the reduction process. Pellet B exhibited smaller surface cracks and revealed a compact internal structure with irregularities upon division, indicating an inhomogeneous reduction process and internal stress developed during reduction. In the case of Pellet D, surface cracks indicated disruption of the internal structure, and after division, slight layering and porosity were observed, suggesting uniform reduction accompanied by microstructural changes. Pellet C retained its shape, but surface cracks revealed changes within the pellets. After division, significant porosity and layering were observed, which may be related to the faster release of gases during the reduction. In all samples, porosity and cracking were observed, which are a result of internal stresses and structural changes induced by the reduction process.

Table 4. Visual macro and micro observation of pellets after hydrogen reduction.

		Pellet A	Pellet B	Pellet C	Pellet D
Input pellet	Photo				
	Macro				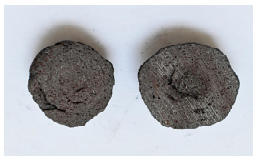
	Micro	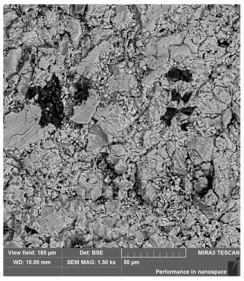	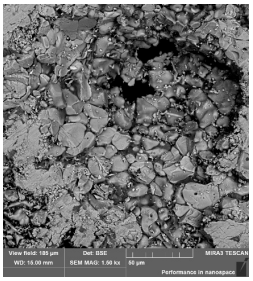	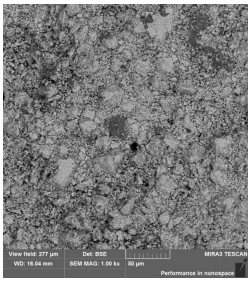	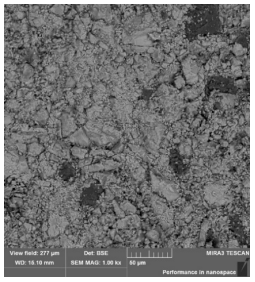
Pellet after H_2 reduction at 600 °C	Photo				
	Macro				
	Micro	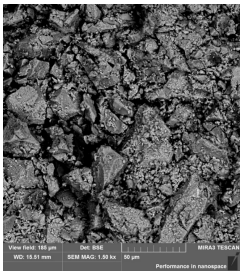	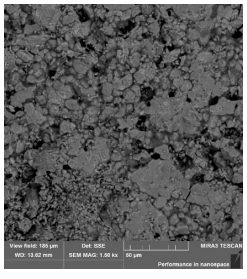	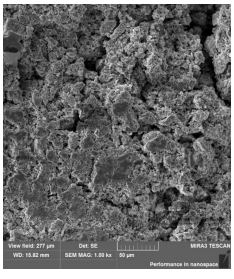	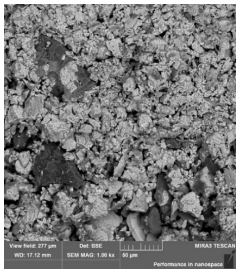

The observation of pellet samples using electron microscopy after reduction at 600 °C in a hydrogen atmosphere was carried out on four different types of pellets. Pellet B reduced at 800 °C was also analyzed separately. Electron microscopy on iron (Fe) pellets after hydrogen reduction was performed for several reasons. Using EDS (energy dispersive spectroscopy), it was possible to analyze the chemical composition of the samples and determine the presence of iron oxides and impurities, which is crucial for optimizing reduction

processes. This method also allowed for the observation of phase changes that occur during the transition from iron oxides to metallic iron and enabled the analysis of their impact on the microstructure of the pellets. Additionally, it enabled the identification of porosity in the pellets after reduction, as this property influences their mechanical characteristics.

The pellet sample A after reduction contains iron oxide (FeO) and reduced iron (Figure 19). The structure of these pellets shows changes in the morphology and shape of the grains compared to the original sample. Small formations based on reduced iron can be found in the structure.

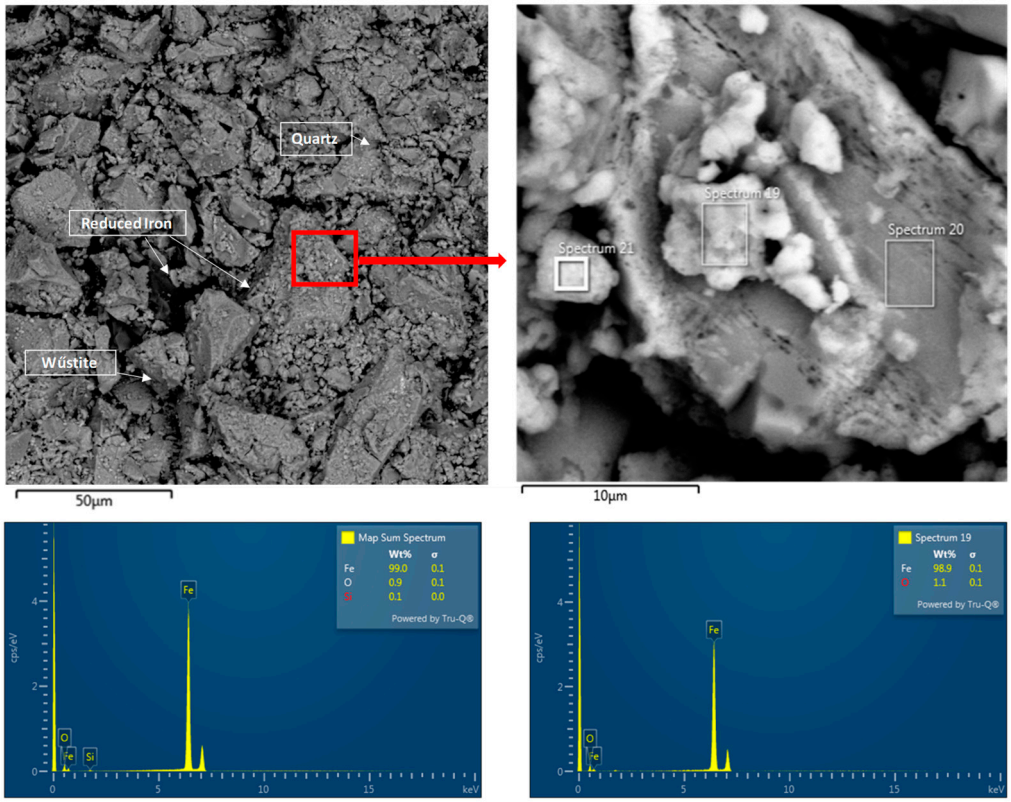

Figure 19. The structure of Pellet A after reduction at 600 °C in an H_2 atmosphere.

Pellet B, reduced at 600 °C, is characterized by the dominant presence of FeO with calcium and silicon impurities but also contains non-reduced areas (Figure 20). Its structure remains similar to the original sample but includes regions with a finer-grained structure, which are associated with the reduced zones. Pellet B after reduction at 800 °C in a hydrogen atmosphere shows the presence of FeO and Fe in the process of reduction to metallic iron and also contains impurities of silicon and calcium. These pellets are characterized by light areas with significantly increased porosity, which arise from the reduced oxides.

Pellet D after reduction at 600 °C in a hydrogen atmosphere shows smaller changes in chemical composition and structure (Figure 21). These pellets contain iron oxides based on Fe_2O_3 (hematite), Fe_3O_4 (magnetite), and FeO, which undergo reduction to elemental iron. The composition also includes iron silicates and silicates with impurities of elements such as Ca, K, and Mg. The structure of these pellets is based on fine-grained formations that protrude to the surface. After reduction, the morphology and shape of the grains changed compared to the original sample.

Pellet C, reduced at 600 °C in a hydrogen atmosphere, contains iron oxides based on FeO, which undergo reduction to metallic iron (Figure 22). There are also areas of metallic iron with impurities of Si and Mg. These pellets' structure is characterized by changes in

the shape and morphology of the grains compared to the original sample, and it includes fine-grained formations based on reduced iron oxides.

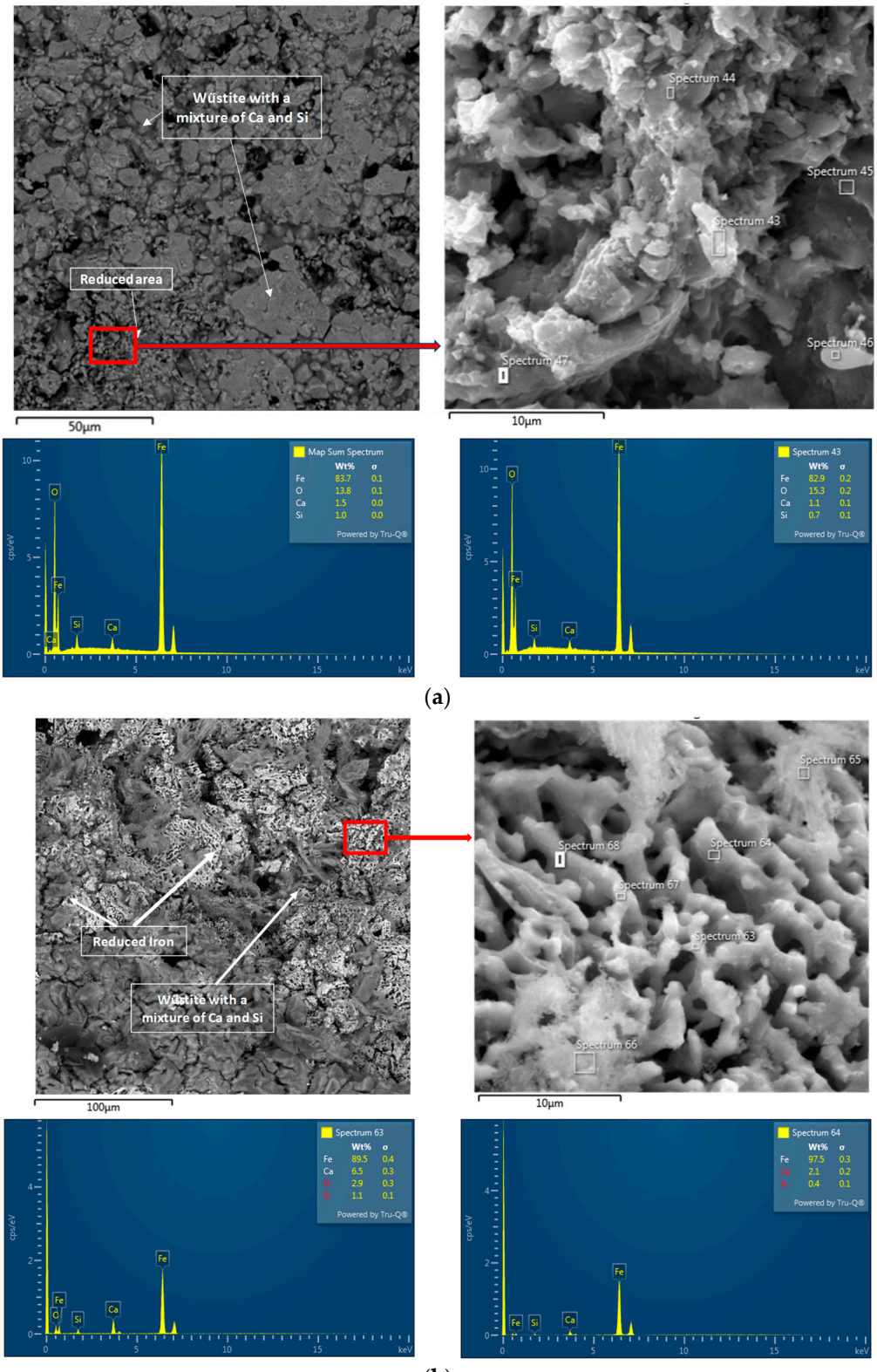

Figure 20. The structure of Pellet B after reduction at (**a**) 600 °C and (**b**) 800 °C in an H_2 atmosphere.

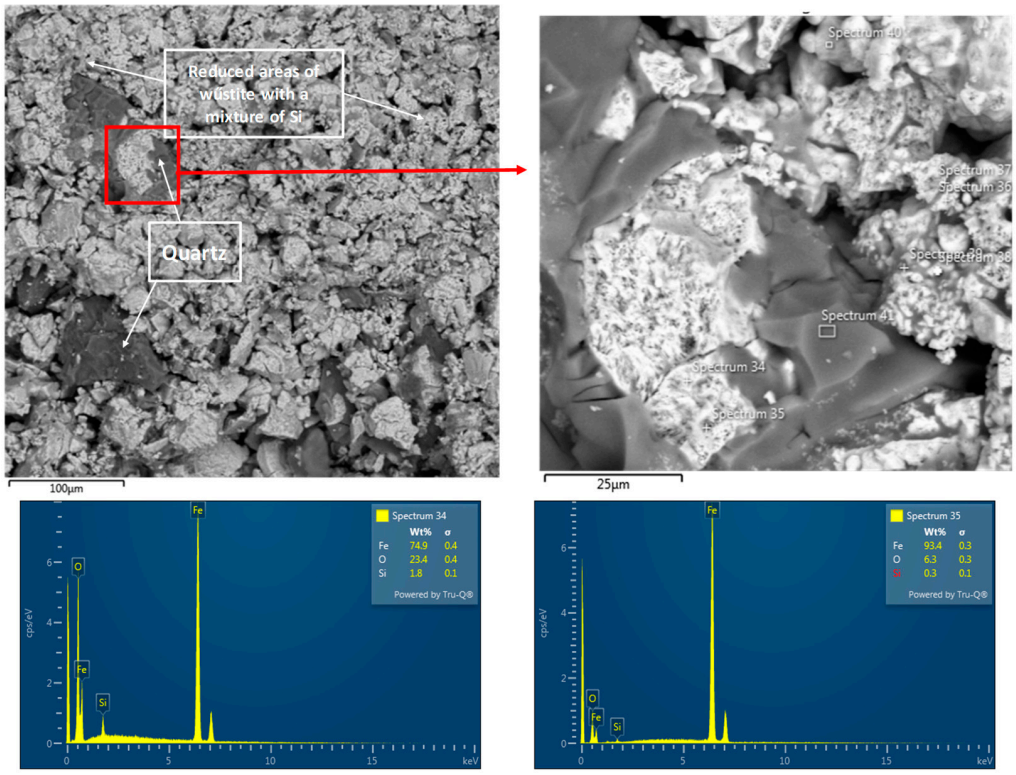

Figure 21. The structure of Pellet D after reduction at 600 °C in an H_2 atmosphere.

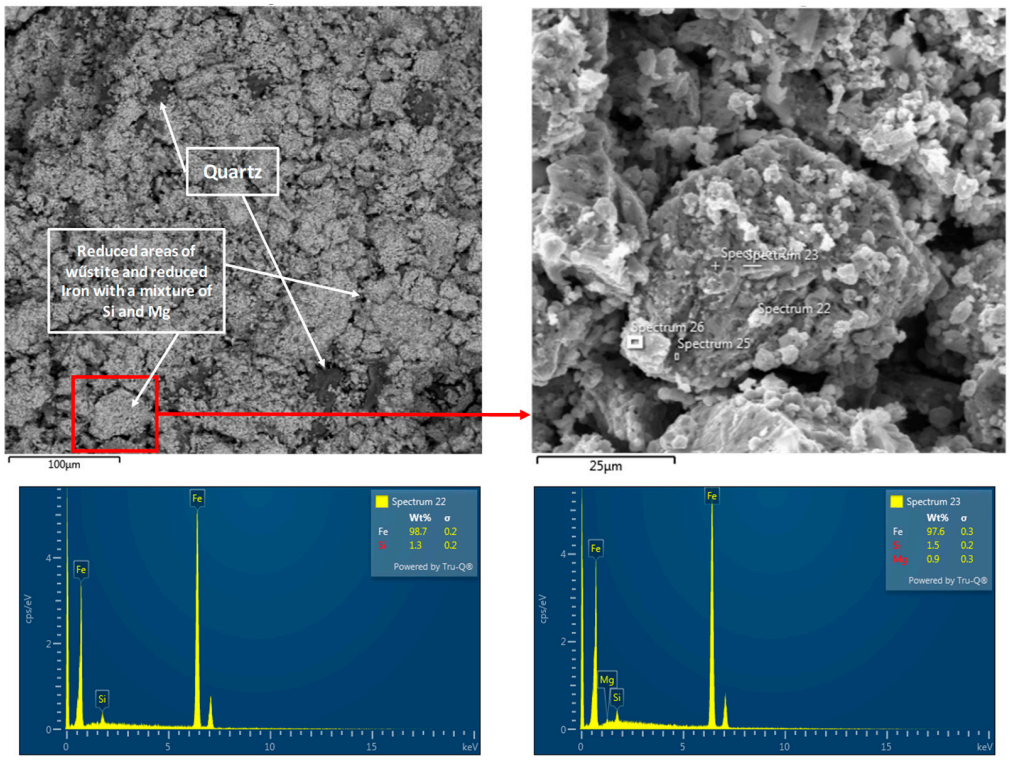

Figure 22. The structure of Pellet C after reduction at 600 °C in an H_2 atmosphere.

Figure 23 schematically illustrates the reduction of iron ore pellets with hydrogen at an experimental temperature of 600 °C. The reduced samples are arranged according to the highest degree of reduction. It is evident that at the reduction temperature of 600 °C, the largest relative increase in Fe_{TOT} content was achieved in Pellets C and A. The structure of these pellets contains a relatively high number of areas with reduced metallic Fe or FeO.

In Pellet A's structure, there are more unreacted grains of original hematite and magnetite compared to Pellet C. On the other hand, the best-reduced Pellet C retains, at the reduction temperature, not only the reduced areas but also the original iron silicate grains, which have not yet decomposed at the experimental temperature of 600 °C, preventing the reduction of FeO from these iron silicates. One of the significant differences in the reduction degree between Pellets C and A may be the higher porosity of Pellet C, which has a very positive effect on the reduction reactions with hydrogen gas. In the case of Pellets D and B, lower reduction degrees and lower relative increases in Fe_{TOT} content were achieved compared to Pellets C and A. In the case of Pellet B, a difficult-to-reduce phase of calcium silicate ferrites from the original pellet was present in the reduced product, which hindered the reduction reactions. Pellets D and B contained a lower proportion of reduced Fe grains and, on the other hand, contained a higher proportion of silicates (in Pellet D, these were iron silicates, and in Pellet B, they were calcium silicate ferrites) compared to Pellets C and A.

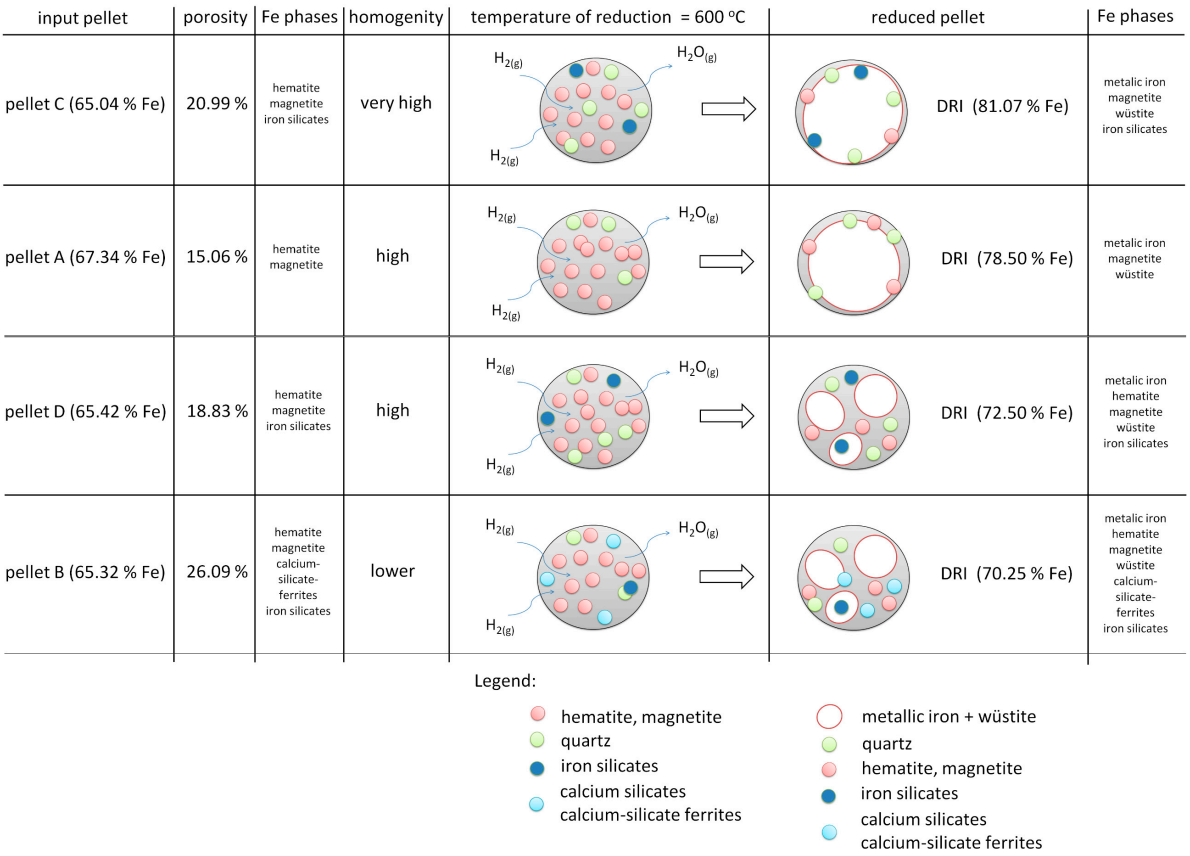

Figure 23. Schematic comparison of the reduction of iron ore pellets.

4. Conclusions

The results of the material research show that the combination of chemical composition, microstructure, and porosity has a decisive impact on the reducibility of pellets. Pellets A and C show the best results in both thermodynamic simulations and experimental tests, suggesting that their optimized chemical and physical properties support an efficient reduction process of iron.

1. The chemical composition of the pellets is a decisive factor for their reducibility. A higher Fe_{TOT} content in Pellets A and C led to better reduction results. The presence of CaO in Pellet B caused the formation of hard-to-reduce phases, such as calcium-silicate ferrites, which decreased their reducibility. A high SiO_2 content in Pellets C and D also negatively affected reducibility due to the formation of iron silicates.

2. Based on thermodynamic models, it was anticipated that Pellet A would achieve the highest reduction, while Pellet B was expected to be the least reducible, confirming the presence of difficult-to-reduce calcium silicate ferrites. Thermodynamic simulations showed that the best reduction results could be achieved at higher temperatures, which was subsequently confirmed in experimental tests at temperatures of 600 °C and 800 °C. The increase in temperature from 600 °C to 800 °C significantly improved the speed and efficiency of the reduction.
3. The microstructural analysis showed that a uniform phase distribution and higher porosity improve the access of the reducing gas to the surface of the particles. Despite expectations, Pellet C achieved better results than Pellet A, which is attributed to its homogeneous microstructure and evenly distributed pores. These findings are crucial when evaluating the reduction potential of pellets at 600 °C and provide valuable insights for further optimization of iron production in industrial conditions.
4. Pellets with higher porosity exhibited a higher degree of reduction due to better hydrogen diffusion. Pellet C, with higher porosity, achieved better results than Pellet A. A homogeneous distribution of pores, as observed in Pellet C, is advantageous for more efficient reduction.
5. The best reducibility results were achieved by Pellets C and A, while Pellet B showed the worst results due to the presence of hard-to-reduce phases. Higher temperatures and homogeneous porosity are key to increasing the reducibility of pellets in pure hydrogen at the observed reduction temperatures.

In conclusion, it can be stated that achieving the highest Fe yields in reduction processes depends on a thorough consideration of the chemical and microstructural properties of pellets, as well as the reduction conditions. This approach can significantly improve energy efficiency and contribute to more effective iron production in industrial processes.

Author Contributions: Conceptualization, Z.M. and J.L.; methodology, R.F.; validation, Z.M., J.L., R.M., A.E. and R.F.; formal analysis, R.D. and R.M.; investigation, Z.M., J.L., R.F., R.D., P.D. and B.B.; resources, Z.M.; data curation, P.D. and B.B.; writing—original draft preparation, Z.M. and J.L.; writing—review and editing, R.F. and R.D.; visualization, R.D., R.M. and A.E.; supervision, R.F.; project administration, J.L. and A.E.; funding acquisition, J.L. and A.E. All authors have read and agreed to the published version of the manuscript.

Funding: This research was funded by the Slovak Research and Development Agency (APVV), Slovak Republic, No. APVV-21-0142, and through the funded project No. AK50VVN0063 by U.S. Steel s.r.o. Košice.

Data Availability Statement: The raw data supporting the conclusions of this article will be made available by the authors on request.

Conflicts of Interest: Authors Andrea Egryová and Róbert Maliňák were employed by the company U. S. Steel Košice, s.r.o. The remaining authors declare that the research was conducted in the absence of any commercial or financial relationships that could be construed as a potential conflict of interest.

References

1. Rosner, F.; Papadias, D.; Brooks, K.; Yoro, K.; Ahluwalia, R.; Autrey, T.; Breunig, H. Green Steel: Design and Cost Analysis of Hydrogen-Based Direct Iron Reduction. *Energy Environ. Sci.* **2023**, *16*, 4121–4134. [CrossRef]
2. Wesseling, J.H.; Lechtenböhmer, S.; Åhman, M.; Nilsson, L.J.; Worrell, E.; Coenen, L. The Transition of Energy Intensive Processing Industries towards Deep Decarbonization: Characteristics and Implications for Future Research. *Renew. Sustain. Energy Rev.* **2017**, *79*, 1303–1313. [CrossRef]
3. Bararzadeh Ledari, M.; Khajehpour, H.; Akbarnavasi, H.; Edalati, S. Greening Steel Industry by Hydrogen: Lessons Learned for the Developing World. *Int. J. Hydrogen Energy* **2023**, *48*, 36623–36649. [CrossRef]

4. Shahabuddin, M.; Brooks, G.; Rhamdhani, M.A. Decarbonisation and Hydrogen Integration of Steel Industries: Recent Development, Challenges and Technoeconomic Analysis. *J. Clean. Prod.* **2023**, *395*, 136391. [CrossRef]
5. Mišković ová, Z.; Legemza, J.; Demeter, P.; Buľko, B.; Hubatka, S.; Hrubovčáková, M.; Futáš, P.; Findorák, R. An Overview Analysis of Current Research Status in Iron Oxides Reduction by Hydrogen. *Metals* **2024**, *14*, 589. [CrossRef]
6. Kazemi, M.; Pour, M.S.; Sichen, D. Experimental and Modeling Study on Reduction of Hematite Pellets by Hydrogen Gas. *Metall. Mater. Trans. B Process Metall. Mater. Process. Sci.* **2017**, *48*, 1114–1122. [CrossRef]
7. Hammam, A.; Nasr, M.I.; Elsadek, M.H.; Khan, I.U.; Omran, M.; Wei, H.; Qiu, D.; Yu, Y. Studies on the Reduction Behavior of Iron Oxide Pellet Fines with Hydrogen Gas: Mechanism and Kinetic Analysis. *J. Sustain. Metall.* **2023**, *9*, 1289–1302. [CrossRef]
8. Korobeinikov, Y.; Meshram, A.; Harris, C.; Kovtun, O.; Govro, J.; O'Malley, R.J.; Volkova, O.; Sridhar, S. Reduction of Iron-Ore Pellets Using Different Gas Mixtures and Temperatures. *Steel Res. Int.* **2023**, *94*, 2300066. [CrossRef]
9. Zakeri, A.; Coley, K.S.; Tafaghodi, L. Microstructural Evolution and Its Effect on Reaction Rate During Reduction of High-Grade Hematite Ore Pellets With Hydrogen. *J. Sustain. Metall.* **2025**, 1–22. [CrossRef]
10. Kovtun, O.; Levchenko, M.; Ilatovskaia, M.O.; Aneziris, C.G.; Volkova, O. Results of Hydrogen Reduction of Iron Ore Pellets at Different Temperatures. *Steel Res. Int.* **2024**, 2300707. [CrossRef]
11. Hessling, O.; Fogelström, J.B.; Kojola, N.; Martinsson, J. Influence of Water Content on the Kinetics and Mechanisms of Hydrogen Reduction Using Industrial Iron Ore Pellets at 873 K–1173 K. *ISIJ Int.* **2024**, *64*, 1493–1502. [CrossRef]
12. Ma, Y.; Souza Filho, I.R.; Zhang, X.; Nandy, S.; Barriobero-Vila, P.; Requena, G.; Vogel, D.; Rohwerder, M.; Ponge, D.; Springer, H.; et al. Hydrogen-Based Direct Reduction of Iron Oxide at 700°C: Heterogeneity at Pellet and Microstructure Scales. *Int. J. Miner. Metall. Mater.* **2022**, *29*, 1901–1907. [CrossRef]
13. Heidari, A.; Ghosalya, M.K.; Alaoui Mansouri, M.; Heikkilä, A.; Iljana, M.; Kokkonen, E.; Huttula, M.; Fabritius, T.; Urpelainen, S. Hydrogen Reduction of Iron Ore Pellets: A Surface Study Using Ambient Pressure X-Ray Photoelectron Spectroscopy. *Int. J. Hydrogen Energy* **2024**, *83*, 148–161. [CrossRef]
14. Mishra, B.; Kumar Singh, A.; Shankar Mahobia, G. Hydrogen Reduction Studies of Low-Grade Multimetallic Magnetite Ore Pellets. *Miner. Eng.* **2024**, *215*, 108823. [CrossRef]
15. Hosseinzadeh, M.; Kasiri, N.; Rezaei, M.; Mohammad Mirzaei, M.A. Investigation of Pellet Shape on the Hydrogen Reduction of Iron Oxide Using Mathematical Modeling and Image Processing. *Steel Res. Int.* **2023**, *94*, 2300085. [CrossRef]
16. Metolina, P.; Ribeiro, T.R.; Guardani, R. Hydrogen-Based Direct Reduction of Industrial Iron Ore Pellets: Statistically Designed Experiments and Computational Simulation. *Int. J. Miner. Metall. Mater.* **2022**, *29*, 1908–1921. [CrossRef]
17. Ali, M.L.; Fradet, Q.; Riedel, U. Kinetic Mechanism Development for the Direct Reduction of Single Hematite Pellets in H2/CO Atmospheres. *Steel Res. Int.* **2022**, *93*, 2200043. [CrossRef]
18. Perrone, A.; Cavaliere, P.; Sadeghi, B.; Dijon, L.; Laska, A.; Koszelow, D. Carburization Behavior of High-Grade Pellets After Direct Reduction in Pure Hydrogen. *J. Sustain. Metall.* **2024**, *10*, 1991–2008. [CrossRef]
19. Cavaliere, P.; Dijon, L.; Laska, A.; Koszelow, D. Hydrogen Direct Reduction and Reoxidation Behaviour of High-Grade Pellets. *Int. J. Hydrogen Energy* **2024**, *49*, 1235–1254. [CrossRef]
20. Cavaliere, P.; Perrone, A.; Dijon, L.; Laska, A.; Koszelow, D. Direct Reduction of Pellets through Hydrogen: Experimental and Model Behaviour. *Int. J. Hydrogen Energy* **2024**, *49*, 1444–1460. [CrossRef]
21. Özgün, Ö.; Dirba, I.; Gutfleisch, O.; Ma, Y.; Raabe, D. Green Ironmaking at Higher H2 Pressure: Reduction Kinetics and Microstructure Formation During Hydrogen-Based Direct Reduction of Hematite Pellets. *J. Sustain. Metall.* **2024**, *10*, 1127–1140. [CrossRef] [PubMed]
22. Perrone, A.; Cavaliere, P.; Sadeghi, B.; Dijon, L.; Laska, A. Optimization of Hydrogen Utilization and Process Efficiency in the Direct Reduction of Iron Oxide Pellets: A Comprehensive Analysis of Processing Parameters and Pellet Composition. *Steel Res. Int.* **2024**, *96*, 2400565. [CrossRef]
23. Kovtun, O.; Levchenko, M.; Oldinski, E.; Gräbner, M.; Volkova, O. Swelling Behavior of Iron Ore Pellets during Reduction in H2 and N2/H2 Atmospheres at Different Temperatures. *Steel Res. Int.* **2023**, *94*, 2300140. [CrossRef]
24. Sharma, T.; Gupta, R.C.; Prakash, B. Effect of Gangue Content on the Swelling Behaviour of Iron Ore Pellets. *Miner Eng.* **1990**, *3*, 509–516. [CrossRef]
25. Meshram, A.; Korobeinikov, Y.; Wei, X.; OMalley, R.J.; Sridhar, S. Quantification of Swelling in Hematite Pellets Reduced Using Hydrogen–Nitrogen Gas Mixture. *Steel Res. Int.* **2024**, 2400442. [CrossRef]
26. Nyankson, E.; Kolbeinsen, L. Kinetics of Direct Iron Ore Reduction with CO-H2 Gas Mixtures. *Int. J. Eng. Res. Technol.* **2015**, *4*, 934–940. [CrossRef]
27. Devlin, A.; Kossen, J.; Goldie-Jones, H.; Yang, A. Global Green Hydrogen-Based Steel Opportunities Surrounding High Quality Renewable Energy and Iron Ore Deposits. *Nat. Commun.* **2023**, *14*, 2578. [CrossRef]
28. Zhang, X.; Fan, Z.; Mi, A.; Cong, J.; Hu, Z.; Yang, J.; Wen, B. Characteristics of NH3–H2 Reducing Pellets. *Metals* **2024**, *14*, 1314. [CrossRef]

29. ANSYS FLUENT Tutorial Guide | PDF. Available online: https://www.slideshare.net/slideshow/ansys-fluent-tutorial-guide/259648143 (accessed on 20 November 2024).
30. Liu, W.; Zuo, H.; Wang, J.; Xue, Q.; Ren, B.; Yang, F. The Production and Application of Hydrogen in Steel Industry. *Int. J. Hydrogen Energy* **2021**, *46*, 10548–10569. [CrossRef]

Disclaimer/Publisher's Note: The statements, opinions and data contained in all publications are solely those of the individual author(s) and contributor(s) and not of MDPI and/or the editor(s). MDPI and/or the editor(s) disclaim responsibility for any injury to people or property resulting from any ideas, methods, instructions or products referred to in the content.